

# Third-order elasticity of transversely isotropic field shales

Audun Bakk<sup>1</sup>  | Marcin Duda<sup>1</sup>  | Xiyang Xie<sup>1</sup>  | Jørn F. Stenebråten<sup>1</sup>  |  
 Hong Yan<sup>2</sup>  | Colin MacBeth<sup>3</sup>  | Rune M. Holt<sup>1,2</sup> 

<sup>1</sup>Department of Applied Geoscience, SINTEF, Trondheim, Norway

<sup>2</sup>Department of Geoscience and Petroleum, Norwegian University of Science and Technology, Trondheim, Norway

<sup>3</sup>Institute of GeoEnergy Engineering, Heriot-Watt University, Edinburgh, UK

## Correspondence

Audun Bakk, Department of Applied Geoscience, SINTEF, S.P. Andersens veg 15B, 7031 Trondheim, Norway.  
 Email: audun.bakk@sintef.no

## Funding information

The Research Council of Norway, Grant/Award Numbers: 234074, 294369; AkerBP ASA; Equinor ASA; Shell Global Solutions B.V.; Vår Energi ASA; INEOS Energy; TotalEnergies

## Abstract

The formations above a producing reservoir can exhibit large mechanical changes, creating a risk of significant subsidence and loss of rock integrity. These changes can be monitored by time-lapse seismic acquisition, which measures the corresponding velocity changes via time-shifts. Third-order elastic theory can be used to connect subsurface strains and stress changes to these seismic attribute changes. Existing models assume isotropic strain dependence of the dynamic stiffness in shales. It is important to re-evaluate this isotropic assumption considering the inherent anisotropy of shales and their abundance in the overburden. Thus, we instead propose a third-order elastic model with a transversely isotropic strain dependence of the dynamic stiffness. When calibrated, this new model satisfactorily predicted P-wave velocity changes determined in undrained laboratory experiments conducted on overburden field shales, covering a wide range of propagation directions and stress variations. The shales exhibit anisotropic dynamic strain sensitivity, resulting in a significantly higher strain sensitivity predicted for Thomsen's anisotropy parameters epsilon and delta subjected to a uniaxial strain parallel to the horizontal bedding plane compared to the vertical direction. Geomechanical modelling, considering a depleting disk-shaped reservoir surrounded by shales, was employed to predict the dynamic stiffness changes of the overburden using the laboratory-calibrated third-order elastic model. The overburden time-shifts increased with offset angle, peaking at about 45°, suggesting a strong influence of shear strains on the time-shifts. In contrast, a corresponding model with an isotropic third-order elastic tensor, calibrated to the same data, exhibited a significantly lower sensitivity to the shear strains. These results underscore the importance of considering the anisotropic strain dependence of the dynamic stiffness when studying shales. Interpreting offset-dependent trends in pre-stack time-lapse seismic data, along with geomechanical modelling and an appropriate strain-dependent rock physics model, can assist in quantifying subsurface strains and stress changes.

## KEYWORDS

acoustics, anisotropy, rock physics, seismics, time lapse

This is an open access article under the terms of the Creative Commons Attribution-NonCommercial-NoDerivs License, which permits use and distribution in any medium, provided the original work is properly cited, the use is non-commercial and no modifications or adaptations are made.

© 2024 The Authors. *Geophysical Prospecting* published by John Wiley & Sons Ltd on behalf of European Association of Geoscientists & Engineers.



## INTRODUCTION

Experiments show that velocities in rocks depend on strain and stress (e.g. Johnston, 1987; Jones & Wang, 1981). Most of the rocks in the crust are anisotropic (Crampin et al., 1984; Helbig & Thomsen, 2005; Thomsen, 1986; Tsvankin, 1997). Shales, frequently encountered in the overburden, exhibit inherent anisotropy and are significantly stress-sensitive. This results in substantial velocity changes that depend on angle and stress path, which is commonly defined as the ratio between horizontal and vertical stress variations (Bakk, Holt, Bauer, et al., 2020; Bauer et al., 2008; Herwanger & Koutsabeloulis, 2011; Holt et al., 2018; Hornby, 1998; Peruvkhina et al., 2008; Sarout & Guéguen, 2008; Scott, 2007). The first time-lapse seismic studies at Ekofisk (Hall et al., 2002) and Valhall (Guilbot & Smith, 2002) demonstrated a significant strain dependence of velocities in the overburden. Thus, 4D seismic data are influenced not only by the changes in the reservoir itself but also by the induced geomechanical changes in the overburden manifested as time-shifts (De Gennaro et al., 2008; Hatchell & Bourne, 2005; Hawkins, 2008; Herwanger & Horne, 2009; Hodgson, 2009; Kenter et al., 2004; MacBeth et al., 2018; Røste & Ke, 2017).

By integrating geomechanical data and rock physics models, 4D seismic data have a significant potential in quantifying strains and stress changes. The compaction of the reservoir can have a critical impact on the overburden, influencing sea-floor subsidence (Angus et al., 2015; Barkved et al., 2005), fault integrity (Kristiansen et al., 2005; Zoback & Zinke, 2002) and well stability both during drilling (Ditlevsen et al., 2018) and in cased holes (Ewy, 2021). The 'R-factor' model, which assigns a constant ratio between the fractional vertical P-wave velocity change and the vertical strain (Hatchell & Bourne, 2005; Røste et al., 2006), has been widely used. Although simplified empirical models can offer valuable insight into dominating trends, more refined models are often needed to understand and predict the behaviour of the rocks in more detail. Anisotropic micromechanical models for dynamic stiffness, often based on cracks and inclusions, have long been popular due to their ability to link the physics at different length scales (Hudson, 1981; Mavko et al., 1995; Sayers & Kachanov, 1995). The effective TOE models constitute another significant group of models (Fuck & Tsvankin, 2009; Hughes & Kelly, 1953; Prioul et al., 2004; Rasolofosaon, 1998; Shapiro, 2017; Sinha & Kostek, 1996; Thurston & Brugger, 1964; Winkler & Liu, 1996). The TOE theory provides a constitutive framework for quantification of the dynamic stiffness changes resulting from strains and stresses exerted on rocks. Sripanich et al. (2021) showed that the TOE coefficients are connected to adiabatic pressure derivatives of elastic moduli. The TOE model proposed by Prioul et al. (2004) assumes isotropic symmetry of the third-order tensor, resulting in a strain sensitivity of the dynamic stiffness that is independent of direction. This model has been cali-

brated to ultrasonic data obtained from different lithologies (Prioul & Lebrat, 2004; Prioul et al., 2004) and has been utilized to predict the seismic response (Asaka, 2023; Fuck et al., 2009; Herwanger & Koutsabeloulis, 2011; MacBeth et al., 2018). Apart from Duda et al. (2020) and Bakk, Holt, Duda et al. (2020), who studied a model with hexagonal symmetry of the TOE tensor, restricted to isotropic horizontal strains, only isotropic TOE tensors have been employed in the modelling of sedimentary rocks (Asaka, 2023; Donald & Prioul, 2015; Fuck et al., 2009; Prioul & Lebrat, 2004; Prioul et al., 2004; Rasolofosaon, 1998; Sarkar et al., 2003; Sinha & Kostek, 1996; Winkler & Liu, 1996). To our knowledge, a transversely isotropic (TI) symmetric TOE tensor has not been previously proposed for any application. Anisotropic TOE tensors are important because of the anisotropic behaviour of sedimentary rocks, particularly overburden shales. Such models can give insight into the time-shift dependency on offset and azimuth. This can benefit the interpretation of both pre-stack and post-stack time-lapse data and thereby improve the quantification of strains and stress changes. It is therefore important to quantify the extent of third-order anisotropy in rocks and to compare predictions obtained from anisotropic TOE tensors with those from isotropic TOE tensors, as addressed in this study.

In this work, we propose an anisotropic model with TI symmetry of the TOE tensor. The elastic coefficients of this model, as well as those of the corresponding model with an isotropic TOE tensor, were determined using ultrasonic experimental data from three different field shales. The fit of the TOE models to the experimental data is discussed in terms of velocity changes as a function of ray angle, relative to the symmetry axis of the rock, and stress path. To examine the TOE models in relation to 4D seismic data, a finite-element geomechanical modelling case was studied, featuring a depleting reservoir surrounded by an anisotropic medium populated by the properties of the experimentally tested shales. The resulting strains from the modelling were used in conjunction with the model to calculate angular variations of time-shifts, demonstrating their dependency on the symmetry of the TOE tensor.

The novelty of the present work is as follows: (1) development of an anisotropic TOE tensor with TI symmetry that accommodates the complete strain tensor; (2) calibration of the TOE coefficients to laboratory data from different overburden field shales; and (3) discussion of angular time-shift trends for a geomechanical modelling case with both TI and isotropic symmetries of the TOE tensor.

## THIRD-ORDER ELASTIC MODEL

In this section, the anisotropic third-order elastic (TOE) stiffness tensor with TI symmetry is developed. The TOE theory enables prediction of how velocities depend on strain. The

expansion of the elastic strain energy of a medium around a reference state of zero strain, truncating at the third-order terms, takes the common form (Brugger, 1964; Fuck & Tsvankin, 2009; Lubarda, 1997; Rasolofosaon, 1998; Shapiro, 2017; Sinha, 1982; Thurston, 1974; Wang & Schmitt, 2021)

$$W = \frac{1}{2} C_{ijkl} \varepsilon_{ij} \varepsilon_{kl} + \frac{1}{6} C_{ijklmn} \varepsilon_{ij} \varepsilon_{kl} \varepsilon_{mn}, \quad (1)$$

where  $C_{ijkl}$  and  $C_{ijklmn}$  are coefficients of the second-order elastic (SOE) and TOE stiffnesses, respectively,  $\varepsilon_{ij}$  are the strain components, and  $i, j, k, l, m$  and  $n$  are dummy indices where summation over repeated indices in each term is implied. Note that the strains in the experiments and simulations herein are of the order  $10^{-3}$  or less, that is infinitesimal. Thus, we will disregard nonlinear terms in the strain itself (albeit *not* in the strain energy in Equation (1), which can be expressed in terms of spatial coordinates  $x_i$  and displacements  $u_i$  as (Fjær et al., 2021, p. 21)

$$\varepsilon_{ij} = \frac{1}{2} \left( \frac{\partial u_i}{\partial x_j} + \frac{\partial u_j}{\partial x_i} \right). \quad (2)$$

Strain is defined positive for compression. The TOE theory was initially applied to crystals where the unstrained configuration may serve as an appropriate reference state (Thurston, 1974, p. 216). Given our focus on field shales, the reference configuration is more naturally that with initial in situ stress and pore pressure. The reference and strained states are hereinafter called the baseline and monitor states, respectively.

For convenience, we adopt Voigt notation, also called abbreviated notation or engineering notation. The tensor components  $\varepsilon_{ij}$  of the strain are expressed as vector components  $e_I$  in Voigt notation:

$$[\varepsilon_{11}, \varepsilon_{22}, \varepsilon_{33}, 2\varepsilon_{23}, 2\varepsilon_{13}, 2\varepsilon_{12}]^T \equiv [e_1, e_2, e_3, e_4, e_5, e_6]^T, \quad (3)$$

where the superscript T stands for transposed. In Voigt notation, the strain energy expanded to the third-order becomes (Brugger, 1964)

$$W = \frac{1}{2} \sum_I C_{II} e_I^2 + \sum_{I < J} C_{IJ} e_I e_J + \frac{1}{6} \sum_I C_{III} e_I^3 + \frac{1}{2} \sum_{I \neq J} C_{III} e_I^2 e_J + \sum_{I < J < K} C_{IJK} e_I e_J e_K, \quad (4)$$

where the subscripts run from 1 to 6. The SOE and TOE tensors possess permutation symmetry, that is  $C_{IJ} = C_{JI}$  and  $C_{IJK} = C_{JIK} = C_{KIJ}$ .

The coordinate systems of the strain tensor and the medium's baseline symmetry must align. Nevertheless, an anisotropic strain implies asymmetry of the effective stiff-

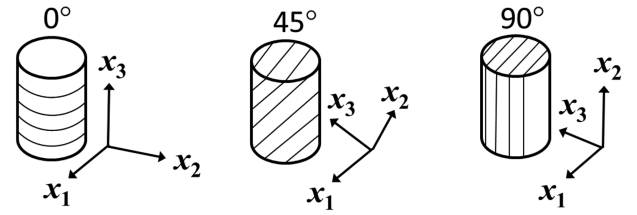


**FIGURE 1** Schematic illustration of the different samples at 0°, 45° and 90° relative to the TI symmetry axis ( $x_3$ ). The bedding is in the  $[x_1, x_2]$  plane.

ness tensor of the strained medium. Thurston (1974, p. 227) referred to this phenomenon as the ‘stretched-string effect’. This is a fundamental difference from an unstrained anisotropic medium implying symmetric effective stiffness. Yet, the asymmetry in monitor stiffness is relatively small as the stress change is much smaller than both the second- and third-order stiffness terms, as highlighted by several authors (Fuck & Tsvankin, 2009; Fuck et al., 2009; Prioul et al., 2004; Rasolofosaon, 1998; Thurston, 1974), and also observed here. Thus, we disregard any asymmetry of the effective stiffness in our analysis. Consequently, the effective monitor stiffness for small amplitude waves becomes (Fuck & Tsvankin, 2009; Prioul et al., 2004; Shapiro, 2017)

$$C_{IJ}^m = C_{IJ} + C_{IJK} e_K. \quad (5)$$

In Voigt notation, the SOE coefficients (baseline stiffnesses) can be represented by a  $6 \times 6$  matrix, and the TOE coefficients can be represented by a  $6 \times 6 \times 6$  matrix or equivalently a six-component vector composed of  $6 \times 6$  matrices. The principle of invariance of the strain energy with respect to transformations implies, at most, 21 independent SOE coefficients and 56 independent TOE coefficients (Brugger, 1965; Fumi, 1951, 1952; Hearmon, 1953).

In this work, we study shales with TI properties, as addressed further below. The hexagonal SOE tensor, which also possesses TI symmetry as proved below, has five independent coefficients:  $C_{11}$ ,  $C_{13}$ ,  $C_{33}$ ,  $C_{44}$  and  $C_{66}$ , as chosen here. The constraint on the last non-vanishing SOE coefficient is (e.g. Fjær et al., 2021, p. 60)

$$C_{12} = C_{11} - 2C_{66}. \quad (6)$$

Although the constraints of the hexagonal TOE tensor are known (Fumi, 1952), it does not possess the required TI symmetry (Fuck & Tsvankin, 2009). To further constrain the hexagonal TOE tensor to TI symmetry, a TI medium with a symmetry axis along  $x_3$  is considered (Figure 1). The axis orientation and notation ( $x_i$ ) refer to the coordinate system of the material symmetry in the baseline state. Hearmon (1953) noted that the constraints on the isotropic TOE coefficients

could be obtained by combining the highest symmetries in the cubic and hexagonal systems. A similar reasoning may be used for the TI system, for which isotropy is only required in the  $[x_1, x_2]$  plane. We generalize the method of Hearmon (1953) by hypothesizing that TI symmetry is obtained by combining the maximum symmetries in the tetragonal and hexagonal systems. This effectively adds a fourfold symmetry axis along  $x_3$  in the hexagonal system. Thus, one new constraint emerges as compared to the hexagonal TOE tensor,  $C_{166} = C_{266}$ . The number of independent third-order coefficients in the TI system is nine:  $C_{111}$ ,  $C_{113}$ ,  $C_{133}$ ,  $C_{144}$ ,  $C_{166}$ ,  $C_{333}$ ,  $C_{344}$ ,  $C_{366}$  and  $C_{456}$ , as chosen here, which are subject to the following constraints:

$$\begin{aligned}
 C_{112} &= C_{122} = C_{111} - 4C_{166}, \\
 C_{123} &= C_{113} - 2C_{366}, \\
 C_{222} &= C_{111}, \\
 C_{223} &= C_{113}, \\
 C_{233} &= C_{133}, \\
 C_{244} &= C_{155} = C_{144} + 2C_{456}, \\
 C_{255} &= C_{144}, \\
 C_{266} &= C_{166}, \\
 C_{355} &= C_{344}.
 \end{aligned} \tag{7}$$

To verify our hypothesis, the strain energy of the system must be invariant to all transformations corresponding to the symmetry (Birch, 1947; Hearmon, 1953). Because the TI TOE system further constrains the hexagonal system, and the constraints on the SOE and TOE coefficients in the hexagonal system are known (Fumi, 1952), it remains to verify the invariance of the strain energy regarding arbitrary rotation around  $x_3$ . This procedure holds valid solely under the approximation of symmetry of the effective stiffness, as previously discussed. The strain energy  $W$  for the TI TOE system is obtained from Equation (4) along with the constraints in Equation (7), resulting in

$$\begin{aligned}
 2W &= C_{11}(e_1 + e_2)^2 + 2C_{13}(e_1 + e_2)e_3 + C_{33}e_3^2 \\
 &+ C_{44}(e_4^2 + e_5^2) + C_{66}(e_6^2 - 4e_1e_2) \\
 &+ \frac{1}{3}C_{111}(e_1 + e_2)^3 + C_{113}(e_1 + e_2)^2e_3 \\
 &+ C_{133}(e_1 + e_2)e_3^2 + C_{144}(e_1 + e_2)(e_4^2 + e_5^2) \\
 &+ C_{166}(e_1 + e_2)(e_6^2 - 4e_1e_2) + \frac{1}{3}C_{333}e_3^3 \\
 &+ C_{344}(e_4^2 + e_5^2)e_3 + C_{366}(e_6^2 - 4e_1e_2)e_3 \\
 &+ 2C_{456}(e_1e_5^2 + e_2e_4^2 + e_4e_5e_6).
 \end{aligned} \tag{8}$$

Consider a clockwise rotation of a strain tensor  $\epsilon$  by an arbitrary angle  $\beta$  around  $x_3$ . The transformed strain tensor is

obtained by (Fjær et al., 2021, p. 687)

$$\begin{bmatrix} \bar{\epsilon}_{11} & \bar{\epsilon}_{12} & \bar{\epsilon}_{13} \\ \bar{\epsilon}_{12} & \bar{\epsilon}_{22} & \bar{\epsilon}_{23} \\ \bar{\epsilon}_{13} & \bar{\epsilon}_{23} & \bar{\epsilon}_{33} \end{bmatrix} = \begin{bmatrix} \cos \beta & \sin \beta & 0 \\ -\sin \beta & \cos \beta & 0 \\ 0 & 0 & 1 \end{bmatrix} \begin{bmatrix} \epsilon_{11} & \epsilon_{12} & \epsilon_{13} \\ \epsilon_{12} & \epsilon_{22} & \epsilon_{23} \\ \epsilon_{13} & \epsilon_{23} & \epsilon_{33} \end{bmatrix} \begin{bmatrix} \cos \beta & -\sin \beta & 0 \\ \sin \beta & \cos \beta & 0 \\ 0 & 0 & 1 \end{bmatrix}. \tag{9}$$

In Voigt notation, the transformed strain is

$$\begin{bmatrix} \bar{e}_1 \\ \bar{e}_2 \\ \bar{e}_3 \\ \bar{e}_4 \\ \bar{e}_5 \\ \bar{e}_6 \end{bmatrix} = \begin{bmatrix} e_1 \cos^2 \beta + e_2 \sin^2 \beta + e_6 \cos \beta \sin \beta \\ e_1 \sin^2 \beta + e_2 \cos^2 \beta - e_6 \cos \beta \sin \beta \\ e_3 \\ \frac{1}{2}(e_4 \cos \beta - e_5 \sin \beta) \\ \frac{1}{2}(e_4 \sin \beta + e_5 \cos \beta) \\ (e_2 - e_1) \cos \beta \sin \beta + \frac{1}{2}e_6(\cos^2 \beta - \sin^2 \beta) \end{bmatrix}. \tag{10}$$

The strain energy in Equation (8) can be recast to

$$\begin{aligned}
 2W &= \left( C_{11} + \frac{1}{3}C_{111}I_1 \right) I_1^2 + \left( C_{33} + \frac{1}{3}C_{333}I_3 \right) I_3^2 \\
 &+ (2C_{13} + C_{113}I_1 + C_{133}I_3) I_1 I_3 \\
 &+ (C_{44} + C_{144}I_1 + C_{344}I_3) I_2 \\
 &+ (C_{66} + C_{166}I_1 + C_{366}I_3) I_4 + 2C_{456}I_5,
 \end{aligned} \tag{11}$$

where

$$\begin{aligned}
 I_1 &= e_1 + e_2, \\
 I_2 &= e_4^2 + e_5^2, \\
 I_3 &= e_3, \\
 I_4 &= e_6^2 - 4e_1e_2, \\
 I_5 &= e_1e_5^2 + e_2e_4^2 + e_4e_5e_6.
 \end{aligned} \tag{12}$$

By substituting  $\bar{e}_I$  from Equation (10) for  $e_I$  in Equation (12), we obtain  $I_i(\bar{\mathbf{e}}) = I_i(\mathbf{e})$  for  $i = \{1, 2, 3, 4, 5\}$ . This means that all five combinations of strain in Equation (12) are specific invariants for the rotation around  $x_3$ . These strain invariants should not be mistaken for the ordinary strain invariants that are applicable to arbitrary transformations of the strain tensor (e.g. Fjær et al., 2021, p. 19). Importantly, this implies that the strain energy in Equation (11) is invariant as well, because  $W(\bar{\mathbf{e}}) = W(\mathbf{e})$ . Thus, the imposition of any rotation around  $x_3$  whatsoever on the strain energy will simply lead to an identity and there can be no further reduction in the number of independent coefficients. This proves that the proposed TOE tensor with nine independent coefficients, along with the constraints in Equation (7), has the required TI symmetry. Furthermore, this supports our hypothesis that constraining the hexagonal system with a fourfold symmetry axis is consistent with TI symmetries for both the SOE and TOE tensors. Hence, the 21 distinct monitor stiffness coefficients for a medium with TI symmetry of both the SOE and

TOE tensors are

$$\begin{aligned}
 C_{11}^m &= C_{11} + C_{111}e_1 + (C_{111} - 4C_{166})e_2 + C_{113}e_3, \\
 C_{12}^m &= C_{11} - 2C_{66} + (C_{111} - 4C_{166})(e_1 + e_2) \\
 &\quad + (C_{113} - 2C_{366})e_3, \\
 C_{13}^m &= C_{13} + C_{113}e_1 + (C_{113} - 2C_{366})e_2 + C_{133}e_3, \\
 C_{14}^m &= C_{144}e_4, \\
 C_{15}^m &= (C_{144} + 2C_{456})e_5, \\
 C_{16}^m &= C_{166}e_6, \\
 C_{22}^m &= C_{11} + (C_{111} - 4C_{166})e_1 + C_{111}e_2 + C_{113}e_3, \\
 C_{23}^m &= C_{13} + (C_{113} - 2C_{366})e_1 + C_{113}e_2 + C_{133}e_3, \\
 C_{24}^m &= (C_{144} + 2C_{456})e_4, \\
 C_{25}^m &= C_{144}e_5, \\
 C_{26}^m &= C_{166}e_6, \\
 C_{33}^m &= C_{33} + C_{133}(e_1 + e_2) + C_{333}e_3, \\
 C_{34}^m &= C_{344}e_4, \\
 C_{35}^m &= C_{344}e_5, \\
 C_{36}^m &= C_{366}e_6, \\
 C_{44}^m &= C_{44} + C_{144}e_1 + (C_{144} + 2C_{456})e_2 + C_{344}e_3, \\
 C_{45}^m &= C_{456}e_6, \\
 C_{46}^m &= C_{456}e_5, \\
 C_{55}^m &= C_{44} + (C_{144} + 2C_{456})e_1 + C_{144}e_2 + C_{344}e_3, \\
 C_{56}^m &= C_{456}e_4, \\
 C_{66}^m &= C_{66} + C_{166}(e_1 + e_2) + C_{366}e_3.
 \end{aligned} \tag{13}$$

The complete TI TOE model in Equation (13) is only valid for a strain tensor with the directional indices referring to the principal coordinate system of the TI baseline state of the medium, which is fulfilled in the laboratory tests as well as in the geomechanical modelling case. In case the medium has a dip in a global reference system, the strain tensor must therefore be oriented in the local (dipping) coordinate system, dictated by the baseline material symmetry, to which the corresponding effective stiffnesses and all derived quantities (e.g. velocities) also pertain. Note that the TI TOE tensor does not generally imply a TI symmetry of the monitor stiffness in Equations (5) and (13), except in cases where the stress change has rotational symmetry around the TI symmetry axis. In our modelling scenarios, and in field cases in general, the principal strain (and stress change) tensor can take any orientation. The symmetry of the strained medium depends on the symmetry of the TOE tensor and the structure of the strain tensor, as pointed out by Fuck and Tsvankin (2009), as well as the symmetry of the SOE tensor. It is also worth mentioning that the model in Equation (13) can alternatively accommodate any symmetry of the baseline stiffness  $C_{IJ}$ , although assuming equal symmetry in the second- and third-order tensors is a natural choice in most cases. If the baseline tensor has lower symmetry than the third-order TI stiffness, the complete elastic tensor, including the second- and third-order terms, will have lower symmetry than TI. However,

this does not violate the derived constraints on the TI TOE parameters.

The corresponding model with isotropic TOE tensor (isotropic TOE model) has three independent isotropic TOE coefficients:  $C_{111}^{\text{iso}}$ ,  $C_{113}^{\text{iso}}$  and  $C_{144}^{\text{iso}}$ , as chosen here, along with the constraints (Fuck & Tsvankin, 2009; Hearmon, 1953):

$$\begin{aligned}
 C_{133}^{\text{iso}} &= C_{113}^{\text{iso}}, \\
 C_{333}^{\text{iso}} &= C_{111}^{\text{iso}}, \\
 C_{166}^{\text{iso}} &= C_{344}^{\text{iso}} = \frac{1}{4}(C_{111}^{\text{iso}} - C_{113}^{\text{iso}}), \\
 C_{366}^{\text{iso}} &= C_{144}^{\text{iso}}, \\
 C_{456}^{\text{iso}} &= \frac{1}{8}(C_{111}^{\text{iso}} - C_{113}^{\text{iso}}) - \frac{1}{2}C_{144}^{\text{iso}}.
 \end{aligned} \tag{14}$$

Note the constraints in Hearmon (1953) need to be transposed because we apply Voigt notation, implying  $C_{ijklmn} = C_{IJK}$  (Brugger, 1964; Fuck & Tsvankin, 2009). The monitor stiffness for the isotropic TOE model is obtained by substituting  $C_{IJK}^{\text{iso}}$  from Equation (14) for  $C_{IJK}$  on the right hand side of Equation (13). By accommodating shear strains, this isotropic TOE model is thus generalizing the model proposed by Prioul et al. (2004).

## METHOD

### Materials, experimental setup and establishment of in situ conditions

All tests follow established geomechanical testing guidelines (Dudley et al., 2016). Samples made of aluminium and polyetheretherketone were used for the static and dynamic calibration of the setup. Laboratory experiments were conducted on three different field shales: M shale, D shale and B shale. After coring at the rig, each shale core, 4 in. in diameter and 12 in. long, was protected using the 'seal peel' method before being safely stored. This involves wrapping the core in plastic film, covering it with aluminium foil and applying a layer of wax. The aluminium foil acts as a vapour barrier and reflects heat during the wax-dipping process. This preservation technique enables the cores to be stored for a long time while retaining their suitability for subsequent testing, as it minimizes the loss of pore fluid that would otherwise cause irreversible damage to the shales. The experimental data from these shales are also discussed by Bakk, Holt, Bauer et al. (2020), Bakk, Holt, Duda et al. (2020), Holt et al. (2018) and Duda et al. (2020). The key characteristics of the shales are summarized in Table 1. Representative samples, drilled next to the samples used in the static and dynamic testing, were used to estimate porosity from water loss upon heating and clay content from XRD analysis. All tests are conducted at room temperature. The field samples have not experienced

**TABLE 1** Geological age, true vertical depth measured from sea-level, porosity, clay content (wt%: weight per cent relative solid mass), in situ vertical stress  $\sigma_Z$ , in situ horizontal stress  $\sigma_H$  and in situ pore pressure  $p_F$  of the tested field shales.

Shale	Geological age	Depth (km)	Porosity (%)	Clay content (wt%)	$\sigma_Z$ (MPa)	$\sigma_H$ (MPa)	$p_F$ (MPa)
M	Middle Miocene	1.4	36	71	27.3	25.9	17.2
D	Eocene	2.5	29	73	50.3	49.2	37.9
B	Early Miocene	3.4	24	76	49.8	47.4	35.0

any heating prior to testing, apart from the in situ formation temperature experienced prior to coring and a slight temporary temperature rise during the waxing procedure for the 'seal peel'.

For each shale, three cylindrical samples, 38 mm in diameter and 50–60 mm long, were drilled at angles of 0°, 45° and 90° relative to the bedding-plane normal (Figure 1). Our selection for where to drill the samples was based on visual inspection and CT images of the cores provided by the operator. This process aims to avoid significant fractures and inhomogeneities, as these can lead to stress concentrations, potentially causing non-elastic (plastic) deformation and failure. These mechanisms are beyond the objectives of our current study, which focuses on elastic deformations. Significant inhomogeneities may also lead to position-dependent strain and wave velocities, making it challenging to determine representative bulk properties due to the presence of different rock domains. This approach is expected to yield results closer to in situ local properties of the shales, as fractures may have resulted from core retrieval or sample handling. A comprehensive assessment of geological features, including layering, structure, fracture systems and faults as experienced in the field, would require additional tests and models that are beyond the scope of the present study. The 0°, 45° and 90° samples were used for the inversion of the static stiffness, whereas the 0° and 90° samples were used for the inversion of the dynamic stiffness. Following drilling, each sample was placed in a heat shrink sleeve for protection and support during trimming and grinding of the end surfaces (Figure 2). All preparation was performed using an inert white oil as cooling and circulation fluid, effectively providing an oil surface on the sample to preserve its natural moisture content and avoid any direct exposure to air, without inducing adverse alterations to the rock matrix or pore fluid. Between preparation and testing, the sample was stored, submerged in an inert white oil, in separate closed-lid containers. During testing, a specially designed Viton rubber sleeve was used to seal the sample from the confining fluid, enabling the application of horizontal stress (Figure 3a). The sleeve also facilitated the insertion of the steel pistons exerting vertical stress to the end faces of the samples, as well as allowing for precise positioning of the horizontal ultrasonic sensors and the horizontal strain cantilevers, all in direct contact with the sample surface.

This stack was finally placed in a triaxial load frame, where the vertical stress and the isotropic horizontal (confining) stress were adjusted independently. Note that the 'vertical' and 'horizontal' directions in the experiments refer to the setup, where the axis of the cylindrical sample was aligned with the vertical direction. The vertical strain was determined as the average value of recordings from three linear variable differential transformers (LVDTs) distributed uniformly azimuthally (every 120°) around the sample. Similarly, horizontal strains were determined by averaging recordings from the strain gauges attached to two orthogonal pairs of cantilevers, positioned in the same horizontal plane, aligned at 45° azimuth relative to the horizontal ultrasonic source-receiver transducer alignments (ray paths). The utilization of redundant strain measurements is a well-established approach for enhancing accuracy. The deviation between the mean strain and the individual strains measured by the LVDTs, respectively, was one order of magnitude smaller than the strain magnitude for the loading and unloading steps. This level of deviation falls within the estimated error of the vertical strain. In the case of horizontal strains, this deviation is reduced to two orders of magnitude smaller than the magnitude of the strain for the loading and unloading steps. Based on the individual strain measurements, there are no indications of significant non-uniformity or bias from the TI symmetry in the considered shale samples (as further discussed below). Pore-pressure control was maintained with access through each piston, with a pore-pressure sensor connected to each piston. Radial and end drains, including the use of a fine metal mesh attached to the sample's circumferential surface, were used during testing to enhance drainage and thereby reduce the time required for pore-pressure equilibration during the drained stages.

We determined ultrasonic velocities using pulse transmission with longitudinal transducers, generating mostly P-waves, and transverse (shear) transducers, generating mostly S-waves. P-wave ultrasonic velocities were measured in multiple ray-path directions, relative to the axis of the cylindrical sample, at 0°, 22° (only used for B Shale), 37°, 47°, 68° and 90° (Figure 3b). All longitudinal transducers were in the same vertical plane. S-wave velocities were measured vertically and horizontally, with the polarization directions illustrated in Figure 4. The horizontal transverse transducers were aligned

**FIGURE 2** Samples drilled normal to the bedding ( $0^\circ$  samples) prior to the mechanical testing. To reduce the possibility of damage before testing, the samples were wrapped in a shrink sleeve at this stage.

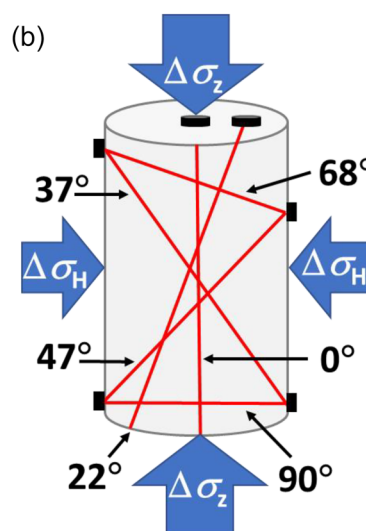
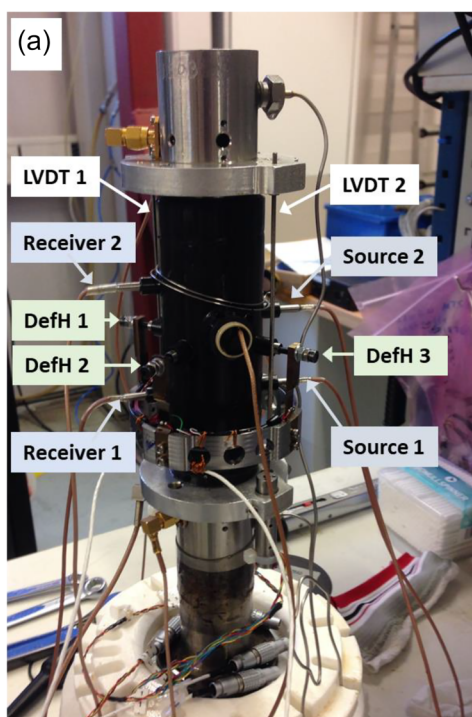
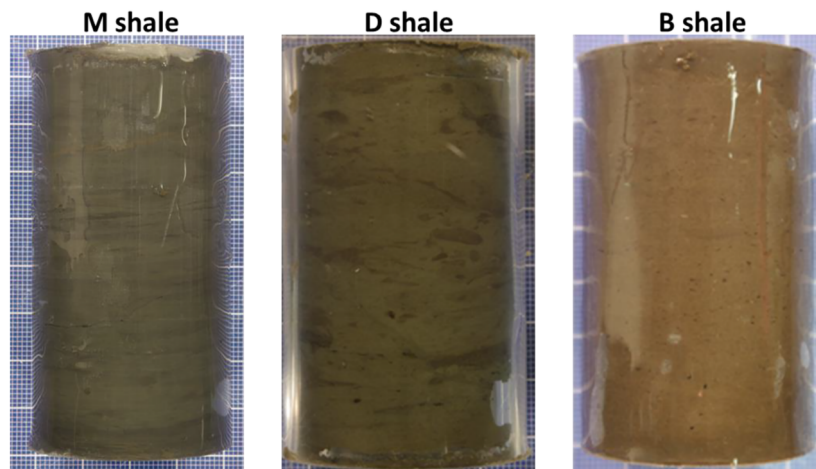


**FIGURE 3** (a) Setup (stack) for the testing prior to mounting in the load frame. The sample is embedded inside the black Viton rubber sleeve. Source/Receiver: longitudinal sources and receivers used for measuring oblique and horizontal P-wave velocities aligned at ray angles:  $37^\circ$ ,  $47^\circ$ ,  $68^\circ$  and  $90^\circ$ , all within the same vertical plane. Longitudinal and transverse transducers aligned at  $0^\circ$  and longitudinal transducers aligned at  $22^\circ$  are integrated in the front of the loading pistons above and beneath the sample. LVDT: linear variable differential transformer for vertical strain measurements (LVDT 3 is hidden). DefH: attachments for two pairs of cantilevers for horizontal strain measurements (DefH 4 is hidden). (b) At the in situ stress and pore pressure, vertical and isotropic (confining) horizontal stress changes were independently exerted on the cylindrical samples according to the different stress paths (Table 2). Ultrasonic P-wave velocities were measured along multiple ray paths (red lines) relative to the axis of the cylindrical sample, constrained by the positions of the transducers (black discs).

at  $90^\circ$  azimuthally relative to the plane defined by the longitudinal transducers. The velocities for the different angles and modes were sampled in a sequence, separated by a delay of a few seconds to avoid any noise (interference) from the preceding sampling. Small ultrasonic longitudinal transducers (2 mm in diameter) for the oblique velocity measurements

were utilized to obtain group velocities directly, as verified by finite-difference wave-propagation simulations (Dellinger & Vernik, 1994; Dewhurst & Siggins, 2006; Hornby, 1998; Larsen et al., 2011; Sarout & Guéguen, 2008). The dominant excitation frequencies for the vertical and non-vertical propagating P-waves were 500 and 600 kHz, respectively,

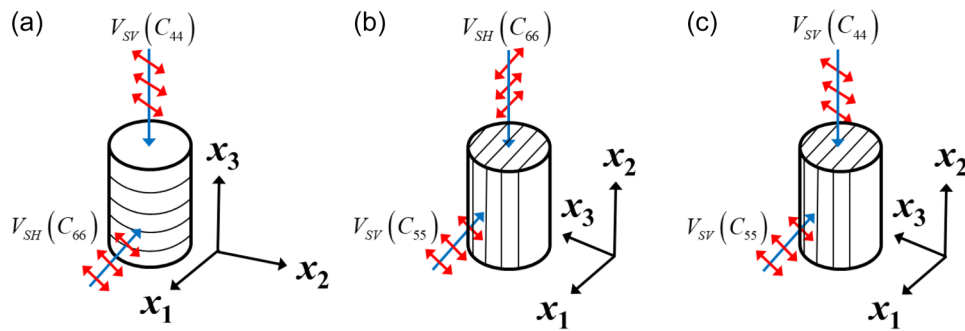


**FIGURE 4** Polarization (red arrows) and propagation direction (blue arrows) of the S-waves obtained in the principal directions: (a) 0° sample test (all samples), (b) 90° sample test for M shale and (c) 90° sample test for D shale. The corresponding determined stiffnesses  $C_{IJ}$  are also indicated.

and 125 kHz for the S-waves. The frequency is determined by the composition and design of the piezoelectric transducers, with transverse transducers requiring a lower frequency, compared to longitudinal transducers, to mitigate the pronounced signal attenuation in shales. At the beginning of the test, the sample was subjected to 5 MPa isotropic stress and 3 MPa pore pressure, whereupon it was exposed to the in situ brine salinity estimated from a pore fluid analysis of the field cores. After consolidation (Dudley et al., 2016; Fjær et al., 2021, p. 73), which involved maintaining a constant and relatively low external stress and allowing drainage of the pore fluid, the sample was loaded in a drained condition to match the estimated in situ stress and pore-pressure values as provided by the field operator (Table 1). Drained conditions mean that the pore pressure is controlled externally by opening the valves to a pump (fluid reservoir) and maintaining a constant (target) pore pressure. A drained loading to in situ stress and pore pressure is expected to lead to full saturation (Dudley et al., 2016). The magnitude of the stress changes applied in our tests (a few MPa) aligns with strain levels typically observed in the vicinity of a depleting reservoir. Therefore, our tests are directly relevant to field conditions. The changes in porosity and density associated with such stress changes are generally small in the surroundings of the reservoir (Holt et al., 2018). A good indication of proper saturation was obtained by determining the undrained pore-pressure response to an isotropic stress change (Skempton, 1954). The corresponding Skempton  $B$  coefficients were as follows: 0.86 for M shale, 0.87 for D shale and 0.83 for B shale. These values align with the expected range for saturated shales (Holt et al., 2018). For undersaturated samples, the Skempton  $B$  coefficients would have been significantly lower (Vernay et al., 2019). Regarding the tests conducted with the 45° and 90° samples, it was not possible to obtain the in situ total stress because the setup was constrained to isotropic horizontal stress. For these samples, the baseline stress was isotropic, equal to the horizontal in situ stress. This bias from in situ vertical stress is not expected to significantly influence the results because the horizontal and

vertical in situ stresses are very close for the tested samples. There was no indication of rock failure in any of the tests.

Transverse isotropy is commonly employed in the study of overburden shales (Asaka, 2023; Delle Piane et al., 2011, 2014; Dewhurst & Siggins, 2006; Hornby, 1998; Johnston, 1987; Jones & Wang, 1981; Sarout & Guéguen, 2008; Thomsen, 1986). However, to conclude, this needs to be experimentally verified. As detailed above, a pair of longitudinal transducers were employed to measure the horizontal P-wave velocity (Figure 3a). The horizontal transverse transducers can then be utilized to quantify possible P-wave anisotropy in the horizontal plane, as they are azimuthally aligned at 90° relative to the horizontal longitudinal transducers. We exploited the fact that the horizontal transverse source inevitably generates a small P-wave signal, which can be recorded as a first arrival by the S-wave receiver. This signal was used to determine the P-wave velocity azimuthally orthogonal to the alignment of the horizontal longitudinal transducer pair. Under constant in situ stress conditions, the azimuthal variation of the P-wave velocity ranged from 10 to 40 m/s for the three shales, which is one order of magnitude lower than the difference between the vertical and horizontal P-wave velocities. This azimuthal variation of the horizontal P-wave velocities falls within the absolute error of the P-wave velocity determination (see the ‘Error analysis’ section). Thus, it is inconclusive whether this slight discrepancy arises from a small deviation from TI symmetry or measurement uncertainties. Also note, the bedding plane of the shales was visually evident, allowing for precise drilling of the samples relative to the bedding-plane normal. These considerations indicate that the conclusion of intrinsic TI symmetry for our field shales is appropriate.

To further assess the consistency of the oblique P-wave velocities with the TI conclusion, we monitored the fit over a 5-h period under constant in situ stress, recording 40–50 data points for each shale. With a maximum variation of 0.05 in Thomsen’s  $\delta$  parameter (Thomsen, 1986), the TI prediction matched all the measured oblique velocities consistently at all



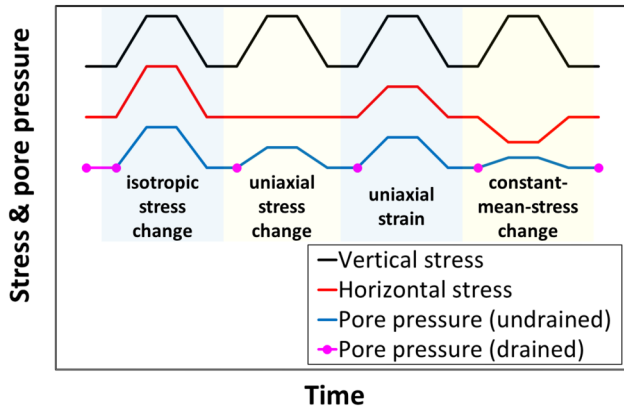


**FIGURE 5** Schematic diagram of the test protocol with the different in situ cycles involving the following stress paths: isotropic stress change, uniaxial stress change, uniaxial strain and constant-mean-stress change. In situ total stresses and pore pressures for the different shales are provided in Table 1, whereas the corresponding stress changes and the number of steps are provided in Table 2. Pore pressure was drained to the in situ value prior to each cycle, ensuring accurate and consistent starting conditions at the in situ pore pressure (indicated by dots). During the stress cycles, the sample was kept undrained. The actual pore-pressure response depends upon the specific material properties, stress path and stress magnitude.

recordings. This observation reinforces the validity of the TI conclusion.

### In situ stress paths

After consolidation at the in situ stress and pore pressure, a sequence of undrained stress cycles involving different stress paths was applied, as schematically shown in Figure 5. Ultrasonic velocity data from the stress cycles were subsequently utilized to calibrate the TOE coefficients. The undrained state imposed during stress cycling is considered realistic for shales due to their low permeability, as further discussed below. The stress cycling involved externally controlled stress paths with stress changes detailed in Table 2, including (1) isotropic stress change, (2) uniaxial stress change, (3) uniaxial strain and (4) constant-mean-stress change. Noteworthy, this leads to a corresponding cycling of the pore pressure due to the undrained conditions (Cheng, 1997). The constant-mean-stress path was included because close to constant mean-stress changes are predicted in a subsurface with equal stiffness of the reservoir and the surrounding rocks (Fjær et al., 2021; Geertsma, 1973, p. 626). One stress cycle consists of following stages:

1. Loading step (5 MPa vertical stress increase), accompanied by a simultaneous change in horizontal (radial confining) stress (different for each stress path, Table 2),

and by a simultaneous corresponding change in pore pressure (undrained response to stress change; not externally controlled).

2. Holding period of 2–4 h for consolidation (pore pressure equilibration).
3. Recording of velocities and strains, as described below.
4. Unloading step, the reverse of the loading step.
5. Holding period of 2–4 h for consolidation.
6. Recording of velocities and strains.

Prior to each stress cycle, the connection between the sample and the pore-pressure intensifier was opened to ensure that all cycles consistently started accurately at the in situ pore pressure.

### Static stiffness from laboratory data

The experimentally determined TI static stiffnesses of the shales were utilized in the geomechanical modelling. Because of the small strains, we assume that the static stiffness is independent of strain. Incorporating finite strain would only result in a marginal correction to the linear strain and would not contribute to the understanding of the overburden dynamic trends of this study. It can be mentioned that finite strains can be accounted for in a static TOE model such as Wang and Schmitt (2021) suggested for isotropic materials. However, this will complicate the calculation of the static model, and consequently also the dynamic TOE model in our case, because a strain implies a change of moduli, which in turn changes the strain.

Hooke's law for the static stiffness  $c$  of a TI medium with the symmetry axis aligned with  $x_3$  is (Fjær et al., 2021, p. 60)

$$\begin{bmatrix} \sigma_1 \\ \sigma_2 \\ \sigma_3 \\ \sigma_4 \\ \sigma_5 \\ \sigma_6 \end{bmatrix} = \begin{bmatrix} c_{11} & c_{11} - 2c_{66} & c_{13} & 0 & 0 & 0 \\ c_{11} - 2c_{66} & c_{11} & c_{13} & 0 & 0 & 0 \\ c_{13} & c_{13} & c_{33} & 0 & 0 & 0 \\ 0 & 0 & 0 & c_{44} & 0 & 0 \\ 0 & 0 & 0 & 0 & c_{44} & 0 \\ 0 & 0 & 0 & 0 & 0 & c_{66} \end{bmatrix} \begin{bmatrix} e_1 \\ e_2 \\ e_3 \\ e_4 \\ e_5 \\ e_6 \end{bmatrix}. \quad (15)$$

Hooke's law for the compliance  $\mathbf{s} \equiv \mathbf{c}^{-1}$  of a TI material is

$$\mathbf{e} = \mathbf{s}\boldsymbol{\sigma}. \quad (16)$$

The static stiffness used in the geomechanical modelling was obtained from three samples drilled at  $0^\circ$ ,  $45^\circ$  and  $90^\circ$  relative to the symmetry axis (Figure 1). From the uniaxial strain along  $x_3$  in the  $0^\circ$  sample, we obtained the vertical uniaxial strain modulus  $H_V$  and the associated  $K_0$  ratio from Equation (15):

$$H_V = \frac{\Delta\sigma_3}{e_3} = c_{33}, e_I = 0 \text{ for } I \neq 3, \quad (17)$$

**TABLE 2** Sample alignment ( $^{\circ}$ ) (Figure 1) and stress changes  $\Delta\sigma_i$  upon vertical loading steps, relative to the in situ (baseline) total stresses in Table 1. For unloading steps, signs of the stress changes were inverted.  $\Delta\sigma(45^{\circ})$ : load along the cylindrical axis of the  $45^{\circ}$  sample; ‘steps’: total number of stress steps.

Stress path	( $^{\circ}$ )	$\Delta\sigma_1$ (MPa)	$\Delta\sigma_2$ (MPa)	$\Delta\sigma_3$ (MPa)	$\Delta\sigma(45^{\circ})$ (MPa)	M shale (steps)	D shale (steps)	B shale (steps)
Isotropic stress change	0	5.0	5.0	5.0	0	4	4	4
Uniaxial strain	0	3.3–3.8 <sup>a</sup>	3.3–3.8 <sup>a</sup>	5.0	0	4	2	4
Uniaxial stress change	0	0	0	5.0	0	4	2	4
Constant-mean-stress change	0	–2.5	–2.5	5.0	0	3	2	4
Uniaxial stress change	45	0	0	0	5.0	4	2	4
Isotropic stress change	90	5.0	5.0	5.0	0	3	4 <sup>b</sup>	4 <sup>b</sup>
Uniaxial stress change	90	0	5.0	0	0	3	4	4 <sup>b</sup>

<sup>a</sup>3.8 MPa for M and D shales; 3.3 MPa for B shale.

<sup>b</sup>Data not utilized here.

$$K_0 = \frac{\Delta\sigma_1}{\Delta\sigma_3} = \frac{c_{13}}{c_{33}}, e_I = 0 \text{ for } I \neq 3. \quad (18)$$

Uniaxial stress change along  $x_3$  in the  $0^{\circ}$  sample test provides the vertical Young’s modulus  $E_V$ , and a uniaxial stress change along  $x_2$  in the  $90^{\circ}$  sample test provides the horizontal Young’s modulus  $E_H$ . From Equation (16) we obtain:

$$E_V = \frac{\Delta\sigma_3}{e_3} = c_{33} - \frac{c_{13}^2}{c_{11} - c_{66}}, \Delta\sigma_I = 0 \text{ for } I \neq 3, \quad (19)$$

$$E_H = \frac{\Delta\sigma_2}{e_2} = \frac{4c_{66} [(c_{11} - c_{66})c_{33} - c_{13}^2]}{c_{11}c_{33} - c_{13}^2}, \Delta\sigma_I = 0 \text{ for } I \neq 2. \quad (20)$$

For a uniaxial stress change at a general angle relative to the symmetry axis, Nye (1985, p. 145) provided Young’s modulus expressed in terms of compliances. Young’s modulus at  $45^{\circ}$ ,  $E_{(45)}$ , which relates a uniaxial stress change  $\Delta\sigma_{(45)}$  and a uniaxial strain  $e_{(45)}$  at  $45^{\circ}$ , can be recast in terms of stiffnesses to

$$E_{(45)} = \frac{\Delta\sigma_{(45)}}{e_{(45)}} = \frac{16c_{44}c_{66} [c_{33}(c_{11} - c_{66}) - c_{13}^2]}{4 [c_{11}c_{33} - c_{13}^2 + c_{44}(c_{11} - c_{13}) - c_{66}(c_{33} + c_{44})] c_{66} + c_{44}(c_{11}c_{33} - c_{13}^2)}. \quad (21)$$

Each of these static quantities,  $H_V$ ,  $K_0$ ,  $E_V$ ,  $E_H$  and  $E_{(45)}$ , was determined as the average value of all steps for the relevant stress path. These quantities were combined within the compound parameter

$$A \equiv \frac{E_V K_0^2 H_V^2}{H_V - E_V}, \quad (22)$$

allowing determination of the five independent TI static stiffness coefficients:

$$c_{11} = A \left( \frac{1}{E_V} + \frac{E_H}{4A - H_V E_H} \right), \quad (23)$$

$$c_{13} = H_V K_0, \quad (24)$$

$$c_{33} = H_V, \quad (25)$$

$$c_{44} = \left( \frac{4}{E_{(45)}} + \frac{H_V K_0}{A} - \frac{1}{E_V} - \frac{1}{E_H} \right)^{-1}, \quad (26)$$

$$c_{66} = \frac{A E_H}{4A - H_V E_H}. \quad (27)$$

The correctness of the expressions for the stiffnesses  $c_{IJ}$  can be verified by inserting the right hand side of Equations (23)–(27) into Equations (17)–(21), respectively.

## Dynamic stiffness from laboratory data

Wave propagation in the symmetry directions of the TI shales, that is in the  $x_3$  direction or in the  $[x_1, x_2]$  plane, implies equal phase velocities and group velocities, and equal phase angles

and group angles (Thomsen, 1986). Thus, the  $C_{11}$ ,  $C_{33}$ ,  $C_{44}$  and  $C_{66}$  (TI) dynamic coefficients, in both the baseline and monitor states, are determined by

$$C_{II} = \rho V_{II}^2, I = \{1, 3, 4, 5, 6\}, \quad (28)$$

where  $\rho$  is the density (corrected for volumetric strain in the monitor state).  $V_{II}$  are the corresponding P- and S-wave group velocities for propagation in the symmetry directions:  $x_1$ , giving  $V_{11} = V_P(90^\circ)$  and  $V_{66} = V_{SH}(90^\circ)$ ;  $x_2$ , giving  $V_{55} = V_{SV}(90^\circ)$ ; and  $x_3$ , giving  $V_{33} = V_P(0^\circ)$  and  $V_{44} = V_{SV}(0^\circ) = V_{SH}(0^\circ)$ , with propagation angles relative to the  $x_3$  symmetry axis (Figure 4a). To determine  $C_{13}$  from the  $0^\circ$  sample test, the oblique group velocities measured at  $22^\circ$  (only for B shale),  $37^\circ$ ,  $47^\circ$  and  $68^\circ$  were additionally utilized (Figure 3b). A complete set of velocities was measured every 30 s. For each set, an optimization routine was run to determine  $C_{13}$ . The ray angle  $\phi$  corresponds to the angle between the straight line connecting the centre positions of the transducer source-receiver pairs and the axis of the cylindrical sample (Figure 3b). For the oblique P-wave velocities, the phase angle  $\theta$  and the phase velocity  $v$  were obtained from Thomsen (1986)

$$\phi = \tan^{-1} \left[ \left( \tan \theta + \frac{1}{v} \frac{\partial v}{\partial \theta} \right) \left( 1 - \frac{\tan \theta}{v} \frac{\partial v}{\partial \theta} \right)^{-1} \right], \quad (29)$$

$$v = \left\{ \frac{1}{2\rho} [C_{33} + C_{44} + (C_{11} - C_{33}) \sin^2 \theta + D] \right\}^{\frac{1}{2}}, \quad (30)$$

with

$$D \equiv \left\{ (C_{33} - C_{44})^2 + 2 \left[ 2(C_{13} + C_{44})^2 - (C_{33} - C_{44})(C_{11} + C_{33} - 2C_{44}) \right] \sin^2 \theta + \left[ (C_{11} + C_{33} - 2C_{44})^2 - 4(C_{13} + C_{44})^2 \right] \sin^4 \theta \right\}^{\frac{1}{2}}. \quad (31)$$

Following Berryman (1979), the scalar magnitude of the group velocity  $V$  was calculated according to

$$V = \left[ v^2 + \left( \frac{\partial v}{\partial \theta} \right)^2 \right]^{\frac{1}{2}}. \quad (32)$$

By minimizing the sum of square deviations between the predicted group velocities and the measured group velocities,  $C_{13}$  was determined (Duda et al., 2020). The theory involved in this routine is valid for arbitrary (*not* just weak) TI anisotropy. Commonly, when determining  $C_{13}$  (or Thomsen's  $\delta$  parameter) in TI rocks, only the  $45^\circ$  direction is

considered beyond the  $0^\circ$  and  $90^\circ$  directions (Delle Piane et al., 2011; Dewhurst & Siggins, 2006; Hornby, 1998; Sarout & Guéguen, 2008). Obtaining a redundancy of oblique P-wave measurements will improve the determination of  $C_{13}$  (Thomsen, 1986), as done in this study. It is also worth noting that there are other methods for inverting stiffnesses in anisotropic media; for example Mah and Schmitt (2003) used an inversion technique based on plane wave decomposition.

### Calibration of third-order elastic coefficients to experimental data

The TOE coefficients were calibrated by optimizing the monitor stiffnesses predicted by Equation (13) with respect to the experimentally determined stiffnesses. In the  $0^\circ$  sample tests, the horizontal (H) strains were isotropic because the principal stress-change tensor was aligned with the symmetry of the TI rock, and only isotropic horizontal stress-changes were exerted on the TI medium, that is,  $e_H \equiv e_1 = e_2$ . There were no shear strains in the coordinate system of the sample because it was vertically aligned with the laboratory setup, where only normal stresses were exerted. Thus, the corresponding (nonzero) independent monitor TI TOE stiffnesses in Equation (13) are

$$\begin{aligned} C_{11}^m &= C_{11} + 2(C_{111} - 2C_{166})e_H + C_{113}e_3 \\ C_{13}^m &= C_{13} + 2(C_{113} - C_{366})e_H + C_{133}e_3 \\ C_{33}^m &= C_{33} + 2C_{133}e_H + C_{333}e_3 \\ C_{44}^m &= C_{44} + 2C_{144}^*e_H + C_{344}e_3 \\ C_{66}^m &= C_{66} + 2C_{166}e_H + C_{366}e_3, \end{aligned} \quad (33)$$

with the compound coefficient

$$C_{144}^* \equiv C_{144} + C_{456}. \quad (34)$$

To determine the TI TOE coefficients, P-wave velocities were measured along all ray paths shown in Figure 3b in addition to horizontal and vertical S-wave velocities for all stress paths in Table 2. As a result, seven out of the nine TI TOE coefficients were determined from the  $0^\circ$  sample data:  $C_{111}$ ,  $C_{113}$ ,  $C_{133}$ ,  $C_{166}$ ,  $C_{333}$ ,  $C_{344}$  and  $C_{366}$ . In addition, the compound coefficient  $C_{144}^*$  was obtained.

The isotropic TOE model was compared with the predictions of the TI TOE model. This is important because only isotropic TOE models were investigated previously. The calibration of the isotropic TOE coefficients,  $C_{111}^{\text{iso}}$ ,  $C_{113}^{\text{iso}}$  and  $C_{144}^{\text{iso}}$ , is uniquely performed with data from the  $0^\circ$  sample test. With the constraints in Equation (14) inserted into Equation (13), the (nonzero) independent monitor stiffnesses utilized for the

calibration of the isotropic TOE coefficients are

$$\begin{aligned}
 C_{11}^{m,iso} &= C_{11} + (C_{111}^{iso} + C_{113}^{iso}) e_H + C_{113}^{iso} e_3, \\
 C_{13}^{m,iso} &= C_{13} + 2(C_{113}^{iso} - C_{144}^{iso}) e_H + C_{113}^{iso} e_3, \\
 C_{33}^{m,iso} &= C_{33} + 2C_{113}^{iso} e_H + C_{111}^{iso} e_3, \\
 C_{44}^{m,iso} &= C_{44} + \left[ C_{144}^{iso} + \frac{1}{4}(C_{111}^{iso} - C_{113}^{iso}) \right] e_H \\
 &\quad + \frac{1}{4}(C_{111}^{iso} - C_{113}^{iso}) e_3, \\
 C_{66}^{m,iso} &= C_{66} + \frac{1}{2}(C_{111}^{iso} - C_{113}^{iso}) e_H + C_{144}^{iso} e_3.
 \end{aligned} \quad (35)$$

Equation (35) is equivalent to the model proposed by Prioul et al. (2004), except they used a different triple of independent isotropic TOE coefficients. Only the TOE coefficients are isotropic in Equation (35), whereas the SOE coefficients have TI symmetry as in the TI TOE model in Equations (13) and (33). This allows for a direct comparison between the TOE tensors with isotropic symmetry and TI symmetry. The coefficients of the TI TOE model in Equation (33) and the isotropic TOE model in Equation (35) are calibrated by iteratively minimizing the residual  $R$ , defined as the sum of square deviations between the monitor stiffness predicted (P) by the model  $C_{IJ}^{m,P}$  and the experimentally (E) determined stiffness  $C_{IJ}^{m,E}$ , summed over all steps:

$$\begin{aligned}
 R = \sum \frac{1}{N_i} \left[ (C_{11}^{m,P} - C_{11}^{m,E})^2 + (C_{13}^{m,P} - C_{13}^{m,E})^2 \right. \\
 \left. + (C_{33}^{m,P} - C_{33}^{m,E})^2 + (C_{44}^{m,P} - C_{44}^{m,E})^2 + (C_{66}^{m,P} - C_{66}^{m,E})^2 \right].
 \end{aligned} \quad (36)$$

Because the number of steps ( $N_i$ ) per stress path ( $i$ ) varied (Table 2), the residual is averaged per stress path, giving equal weight to each of the stress paths in the inversion.

To obtain the remaining TI TOE coefficients  $C_{144}$  and  $C_{456}$ , we utilized the uniaxial stress path cycle in the  $90^\circ$  sample tests to obtain the required strain anisotropy in the  $[x_1, x_2]$  plane ( $e_1 \neq e_2$ ). By substituting  $C_{144}^*$  from Equation (34) into  $C_{44}^m$  and  $C_{55}^m$  in Equation (13), we obtain

$$C_{44}^m = C_{44} + C_{144} e_1 + (2C_{144}^* - C_{144}) e_2 + C_{344} e_3 \quad (37)$$

and

$$C_{55}^m = C_{44} + (2C_{144}^* - C_{144}) e_1 + C_{144} e_2 + C_{344} e_3. \quad (38)$$

Since  $C_{144}^*$  and  $C_{344}$  were calibrated from the  $0^\circ$  sample test, we could determine  $C_{144}^m$  from the  $90^\circ$  sample test. The horizontally propagating S-waves in M shale ( $C_{55}^m$ , Figure 4b), and both the vertically and horizontally propagating S-waves in D shale ( $C_{44}^m$  and  $C_{55}^m$ , Figure 4c) were utilized for the determination of  $C_{144}^m$ . Finally, the ninth TOE coefficient,  $C_{456}$ , could be determined from Equation (34).

## Error analysis

A reference test on aluminium indicates a standard deviation of less than 2% of the static Young's modulus. However, the moduli of shales will in general have less error than measured for aluminium, as aluminium has a Young's modulus of 70 GPa while shales are much softer, implying a larger strain for a given stress. Conservatively, we still assign a standard deviation of 2% for the explicitly determined static quantities,  $H_V$ ,  $E_V$ ,  $E_H$ ,  $E_{(45)}$  and  $K_0$ , in Equations (17)–(21). The errors of the static TI stiffnesses  $c_{IJ}$  are determined through standard error propagation from  $H_V$ ,  $E_V$ ,  $E_H$ ,  $E_{(45)}$  and  $K_0$  to  $c_{IJ}$  in Equations (23)–(27). In the undrained state, there is a small fluid volume (dead volume) between the sample and the closing valves (about 2 mL) that is directly connected to the pore space of the sample. This may lead to an error in the undrained moduli, which is not quantified.

The errors associated with the velocities were estimated from the errors related to the picking of arrival times, sample length, sample radius, stress, strain and temperature. The waveforms and picking of arrivals are discussed in detail by Bakk, Holt, Bauer et al. (2020). All measurements are done in a consolidated (equilibrium) state, and no significant drift in the measurements was observed (see below for details). The standard deviation of the absolute velocities was estimated to be 30 m/s.

This work primarily focuses on velocity changes, which yield distinct error estimates compared to those associated with absolute velocities. For the velocity changes, the error associated with the picking of arrival times is considered the dominant source of error. We analysed 50 consecutive waveforms from a field-shale test over a 25-min interval under constant stress conditions. A standard deviation of 2 m/s was determined, which indicates the picking error. To enhance the accuracy of the determination of the velocity changes, we utilized the average of 10 consecutive velocity measurements (5-min interval) in the consolidated state after each stress change (see the 'In situ stress paths' section). By incorporating smaller errors related to stress, strain and temperature beyond the error estimate for the picking of the arrival times, the standard deviation of the velocity changes is estimated to 2.8 m/s. Based on this error estimate, a Monte Carlo simulation with  $10^6$  inversions of the TOE coefficients was done. In each of these iterations, random errors from a Gaussian distribution were added to the experimentally determined dynamic stiffnesses, respectively. From the distribution of the individual TOE coefficients, the 95% confidence intervals for the TOE coefficients were obtained (Table 4).

For each of the shales, the in situ stress cycles of the  $0^\circ$  tests lasted about 3 days and involved 20–28 steps (10–14 cycles). To assess possible drift in the velocities, the

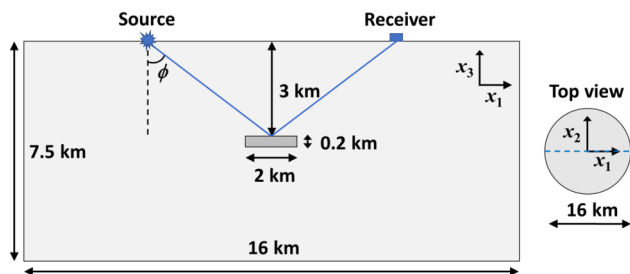


**FIGURE 6** Vertical section intersecting the centre of the axisymmetric geomechanical model. Top horizontal boundary of the disk-shaped reservoir is located at a depth of 3 km. Reservoir has a diameter of 2 km and a thickness of 0.2 km. Straight ray paths in the vertical section  $[x_1, x_3]$  were utilized to quantify two-way traveltimes at different ray angles  $\phi$  from the source to the receiver, via the mid-point reflector at the top of the reservoir. A miniature top view of the entire model in the  $[x_1, x_2]$  plane is shown in the right panel, highlighting the cylindrical boundary of the model, where the intersection of the vertical section is indicated by the broken line.

velocities before the first in situ cycle and after the last in situ cycle step were compared at identical (in situ) stress. The average absolute velocity deviation over a 3-day period, across seven different velocities, was found to be around 2–3 m/s for all three shales. The average volumetric strain per step was of the order of  $10^{-3}$  (absolute value). The difference (absolute value) between the volumetric strain before and after the stress cycles, that is measured at the in situ total stress at both stages, was of the order of  $10^{-5}$  for D and M shales and  $10^{-4}$  for M Shale. This is indicative of a high stability of the acoustic and strain measurements, well-preserved core material, and sufficiently close to elastic behaviour of the rock.

## Geomechanical model

We conducted geomechanical simulations using finite-element software (DIANA FEM), employing an axisymmetric model that includes a depleting disk-shaped reservoir surrounded by shales to represent a simplified field case (Figure 6). This model can highlight useful trends predicted by the TOE tensor related to the angular dependence of time-shifts and time-strains in the overburden, providing insights that are more challenging to attain with a complex geomechanical model. No horizontal displacements were permitted at the vertical (cylindrical) boundary (right panel in Figure 6), whereas no vertical displacements were permitted at the horizontal boundary at the bottom of the model. A free surface was assumed at the horizontal boundary at the top of the model. We simulated the rock's response to a homogeneous pore-pressure reduction (depletion) in the reservoir from 35 MPa (baseline state) to 0 MPa (monitor state). The pore pressure was uniform in the entire reservoir in both the baseline and monitor states. The static drained stiffness of the reservoir is isotropic, and represents a compliant sandstone with

Biot's  $\alpha = 1$  (Fjær et al., 2021, p. 665). Outside the reservoir, homogeneous static (undrained) and dynamic second-order stiffnesses were assigned according to the calibrated values for the three shales (Table 3), respectively, corresponding to the baseline state in each simulation case. For each case, we assigned calibrated TOE coefficients from either the TI TOE model or the isotropic TOE model from Table 4 for the calculation of the monitor stiffness, as explained below. This requires three different geomechanical simulations, resulting in five different scenarios, as the TI TOE tensor was not determined for B shale. It would have been more realistic to have posited spatial variation in properties outside of the reservoir, but this would not have added to understanding the overburden's response to the compacting reservoir within the scope of this study.

## Calculation of overburden time-shifts and time-strains in the modelling case

Homogeneous baseline properties outside the reservoir imply straight ray paths in the baseline state within the overburden. After the depletion, the strain field becomes inhomogeneous. However, with the small strains involved in our study, straight ray paths are also assumed in the monitor state. The modelled strains in the irregular simulation mesh were interpolated onto a fixed regular grid (computational grid) consisting of cubes with an edge length of 50 m. Each grid cell was assigned a homogeneous (interpolated) strain. The computational grid adopts a cylindrical arrangement, representing the physical situation of the axisymmetric model. The boundary of the vertical section  $[x_1, x_3]$  shown in Figure 6 is rectangular and aligns with the boundaries of both the simulation mesh and computational grid. Although the regular grid introduces a small numerical bias with cubic anisotropy in the calculation of time-shifts, these errors have negligible impact on the overall trends discussed in the study. The 50-m computational grid size strikes a balance between ensuring sufficient quality of the interpolated strain data and achieving computational efficiency. We first consider a ray-path segment of baseline length  $L$  at ray angle  $\phi$ . The longitudinal strain of this segment is found by rotating the coordinate system of the strain tensor  $\epsilon$  by an angle  $\phi$  clockwise around  $x_2$ , such that the new (rotated)  $x_3$ -axis becomes aligned with the ray-path segment. This is obtained by the transformation (Fjær et al., 2021, p. 687):

$$\begin{bmatrix} \bar{\epsilon}_{11} & \bar{\epsilon}_{12} & \bar{\epsilon}_{13} \\ \bar{\epsilon}_{12} & \bar{\epsilon}_{22} & \bar{\epsilon}_{23} \\ \bar{\epsilon}_{13} & \bar{\epsilon}_{23} & \bar{\epsilon}_{33} \end{bmatrix} = \begin{bmatrix} \cos \phi & 0 & \sin \phi \\ 0 & 1 & 0 \\ -\sin \phi & 0 & \cos \phi \end{bmatrix} \begin{bmatrix} \epsilon_{11} & \epsilon_{12} & \epsilon_{13} \\ \epsilon_{12} & \epsilon_{22} & \epsilon_{23} \\ \epsilon_{13} & \epsilon_{23} & \epsilon_{33} \end{bmatrix} \begin{bmatrix} \cos \phi & 0 & -\sin \phi \\ 0 & 1 & 0 \\ \sin \phi & 0 & \cos \phi \end{bmatrix}. \quad (39)$$

Thus, the longitudinal (geometric) strain of the ray-path segment becomes in Voigt notation

$$e_{RP} \equiv \bar{\epsilon}_{33} = e_1 \sin^2 \phi + e_3 \cos^2 \phi - e_5 \cos \phi \sin \phi. \quad (40)$$

**TABLE 3** Static (undrained) and dynamic (ultrasonic) second-order elastic stiffnesses of the tested field shales within a 95% confidence interval (in parentheses). Static stiffness of the reservoir sandstone in the modelling case is also included.

Rock	Modulus	$C_{11}$ (GPa)	$C_{33}$ (GPa)	$C_{13}$ (GPa)	$C_{44}$ (GPa)	$C_{66}$ (GPa)
M	Static	7.6 (0.6)	7.3 (0.3)	5.6 (0.3)	0.5 (0.1)	1.3 (0.1)
D	Static	9.7 (0.7)	9.3 (0.4)	7.0 (0.4)	1.0 (0.1)	1.9 (0.2)
B	Static	13.7 (0.8)	10.3 (0.4)	6.7 (0.4)	2.0 (0.1)	4.5 (0.6)
M	Dynamic	13.2 (0.6)	9.9 (0.5)	8.0 (0.9)	1.6 (0.2)	2.9 (0.3)
D	Dynamic	15.7 (0.7)	12.6 (0.6)	9.2 (1.1)	2.0 (0.3)	2.8 (0.3)
B	Dynamic	20.9 (0.8)	15.3 (0.6)	10.2 (1.0)	3.1 (0.3)	5.3 (0.4)
Reservoir	Static	2.4	2.4	1.3	0.6	0.6

**TABLE 4** Calibrated TOE coefficients within a 95% confidence interval (in parentheses) for the TI and isotropic TOE models.

Shale	TOE	$C_{111}$ (GPa) <sup>a</sup>	$C_{113}$ (GPa)	$C_{133}$ (GPa)	$C_{166}$ (GPa)	$C_{333}$ (GPa)	$C_{366}$ (GPa)	$C_{144}$ (GPa)	$C_{344}$ (GPa)	$C_{456}$ (GPa)
M	TI	312 (179)	107 (27)	89 (27)	68 (93)	105 (24)	21 (43)	25 (10)	33 (9)	20 (20)
D	TI	332 (67)	145 (29)	114 (35)	61 (27)	137 (31)	32 (24)	47 (14)	34 (12)	0 (23)
M	Isotropic	94 (17)	57 (18)	57 (18)	9 (25)	94 (17)	11 (12)	11 (12)	9 (25)	-1 (14)
D	Isotropic	145 (27)	104 (29)	104 (29)	10 (40)	145 (27)	-2 (12)	-2 (12)	10 (40)	6 (16)
B	Isotropic	252 (14)	194 (17)	194 (17)	14 (22)	252 (14)	13 (6)	13 (6)	14 (22)	1 (8)

<sup>a</sup>The corresponding unit of strain in Equation (13) is 1.

The time-shift  $\Delta t$  for this segment is

$$\Delta t = t_m - t_b = L \left( \frac{1 - e_{RP}}{V_m(\phi)} - \frac{1}{V_b(\phi)} \right), \quad (41)$$

where  $t$  is the traveltimes and  $V(\phi)$  is the group velocity in the baseline (b) and monitor (m) states at ray angle  $\phi$ . The two-way traveltimes shift  $\Delta T$  is obtained by summing the local two-way traveltimes changes in Equation (41) along the ray path through the computational elements  $I$ :

$$\Delta T = T_m - T_b = \sum_I L_I \left( \frac{1 - e_{RP,I}}{V_m(\phi)} - \frac{1}{V_b(\phi)} \right). \quad (42)$$

The geometric (G) contribution to the time-shift in Equation (42), that is the proportion of the time-shift associated with changes in the seismic path length, is obtained by setting  $V_b(\phi) = V_m(\phi)$ :

$$\Delta T_G = - \sum_I \frac{L_I e_{RP,I}}{V_b(\phi)}. \quad (43)$$

Time-strains, defined as fractional (local) time-shifts, are introduced to quantify the local dynamic alterations (Rickett et al., 2007). The time-strain is obtained from Equation (41)

$$\frac{\Delta t}{t_b} = \frac{V_b(\phi)}{V_m(\phi)} (1 - e_{RP}) - 1. \quad (44)$$

The geometric strain in Equation (43) incorporates the surface (top) displacement where the source and receiver are embedded, which consequently alter positions upon the reservoir depletion. In our case, the horizontal surface strains are particularly small and vanish with increasing angle. This implies that the horizontal displacements of the source and receiver are negligible. In some cases, time-shifts are determined at a fixed offset, that is maintaining identical horizontal distance between the source and receiver in both the baseline and monitor states (e.g. Kudarova et al., 2016; Landrø & Stammeijer, 2004; Røste et al., 2006, 2007). In Appendix A, the corresponding path strain for a fixed offset is provided.

To predict angular time-shifts and time-strains, the baseline velocities were first calculated. At a chosen ray angle  $\phi$ , the corresponding phase angle and phase velocity were obtained by Equations (29) and (30). Subsequently, the group velocity was obtained by Equation (32). It is possible to have a higher symmetry of the monitor stiffness than of the TOE tensor, for example an isotropic strain in a medium with hexagonal SOE and TOE tensors implies TI symmetry of the monitor stiffness (Fück & Tsvankin, 2009). However, in a field case, the symmetry of the monitor stiffness will typically be equal to or lower than the lowest symmetry among the SOE and TOE tensors. Hence, we need to deploy a more robust method to predict velocities for arbitrary symmetry of the monitor stiffness and arbitrary propagation directions. We utilized the open-source Python module *Christoffel* to solve the Christoffel equation to obtain direction-dependent

group velocities (Fedorov, 1968; Jaeken & Cottenier, 2016). The input parameters to the *Christoffel* module included the group angle, monitor stiffnesses in Equation (13) calculated with the strain from the modelling, and the monitor density. The output was the group velocity, which was used to predict angular two-way traveltimes shifts by Equations (42) and (43) and time-strains by Equation (44). The procedure for converting geomechanical data to monitor angular velocities using the TI TOE model can be summarized as follows:

1. Generate the six-component (Voigt) strain vector from a finite-element simulation oriented in the same coordinate system as the principal coordinate system of the rock in the baseline state.
2. Use the strains and the experimentally determined TOE coefficients into Equation (13) to calculate the monitor stiffness.
3. Calculate the monitor group velocity at a given ray angle using the Python module developed by Jaeken and Cottenier (2016).

## RESULTS

### Experimental data

The second-order static and dynamic stiffnesses for the different shales are provided in Table 3. Overall, stiffness increases with depth and decreases with porosity. For M shale, the quality of the horizontal S-wave signal in the 0° sample test was insufficient. Instead, we obtained  $C_{66}$  from the SH-wave velocity measured during the isotropic stress path cycle of the 90° sample test (Figure 1). The TOE coefficients are provided in Table 4. For B shale, the quality of the vertical S-wave velocity change was insufficient (affecting  $C_{44}$ ), such that the TI TOE coefficients could not be determined.

The second-order dynamic moduli are significantly larger than the static moduli. All inverted TI TOE coefficients exhibit a positive value. However, for three of the inverted isotropic TOE coefficients, slightly negative values are obtained. Additionally, for certain TOE coefficients, the confidence intervals exceed the corresponding inverted values. This is plausible since there were no restrictions on the sign during the inversion. Given our strain sign convention, negative signs for some of the third-order coefficients are also reported by Prioul et al. (2004) based on experiments, and Wang and Li (2009) based on ab initio simulations, along with the references cited therein. The fundamental stability criterion for an elastic medium is positive definite elastic energy (Nye, 1985, p. 142). We are not aware of any rigorous bounds for the TOE coefficients. Prioul and Lebrat (2004), who quantified isotropic TOE coefficient for a range

of sedimentary rocks subjected to isotropic stress changes, argued that for *P*- and *S*-waves, stiffnesses mainly respond to the stress in the propagation and polarization directions. For static anisotropy, any bounds derived from this argument will depend on the static stiffness. Given the explicit strain dependence of the TOE model, a similar argument can be made for isotropic strain: for *P*- and *S*-waves, stiffnesses mainly respond to strain in the propagation and polarization directions. By considering  $C_{11}^m$ ,  $C_{33}^m$ ,  $C_{44}^m$ , and  $C_{66}^m$  in Equation (13), this argument implies  $C_{111} > C_{113}$ ,  $C_{166} > 0$ ,  $C_{333} > C_{133}$ ,  $C_{344} > C_{144}$ ,  $C_{166} > C_{366}$ , and  $C_{456} > 0$ . For isotropic TOE coefficients, the first three constraints are identical, and the last three constraints are also identical, implying two distinct constraints. These constraints hold for all shales discussed herein, except for the fourth constraint, which is marginally violated for the isotropic TOE coefficient of M shale and for the TI TOE coefficient of D shale (Table 4). However, it remains to rigorously prove that these constraints are bounds for the TOE coefficients for a given symmetry.

The measured group velocity changes ( $V_m - V_b$ ) due to a 5 MPa vertical stress increase are provided for the different stress paths and ray angles, showing a significant dependency on the stress path (Figure 7). These values are the average of all steps for a given angle and stress path, with the sign of the velocity changes reversed for the vertical unloading steps. The data exhibit relatively flat or slightly decreasing velocity changes with increasing angle for the isotropic stress path and the uniaxial-strain path. The velocity changes decrease significantly with angle for the uniaxial stress path and the constant-mean-stress path, notably reaching negative values at 68° and 90° for the constant-mean-stress path. The latter is caused by a significant expansion of the rock in the ray-path direction. These trends highlight the strong coupling between the stress path and the angular strain dependence of velocities. The TI TOE model demonstrates a good fit to the experimental data, considering the diversity of stress paths and angles involved. The isotropic TOE model overestimates the velocity changes for the triaxial stress path and the constant-mean-stress path for all three shales, whereas for M and D shales, the velocity changes for the isotropic stress path and the uniaxial-strain path are underestimated. Despite the quantitative limitations, the isotropic TOE model qualitatively predicts the angular trends of the velocity changes satisfactorily for all stress paths.

### Geomechanical modelling

The results based on the modelling data are only considered within the vertical section  $[x_1, x_3]$  that intersects the symmetry axis of the reservoir (Figure 6). The strains in the surroundings are most significant near the reservoir, with

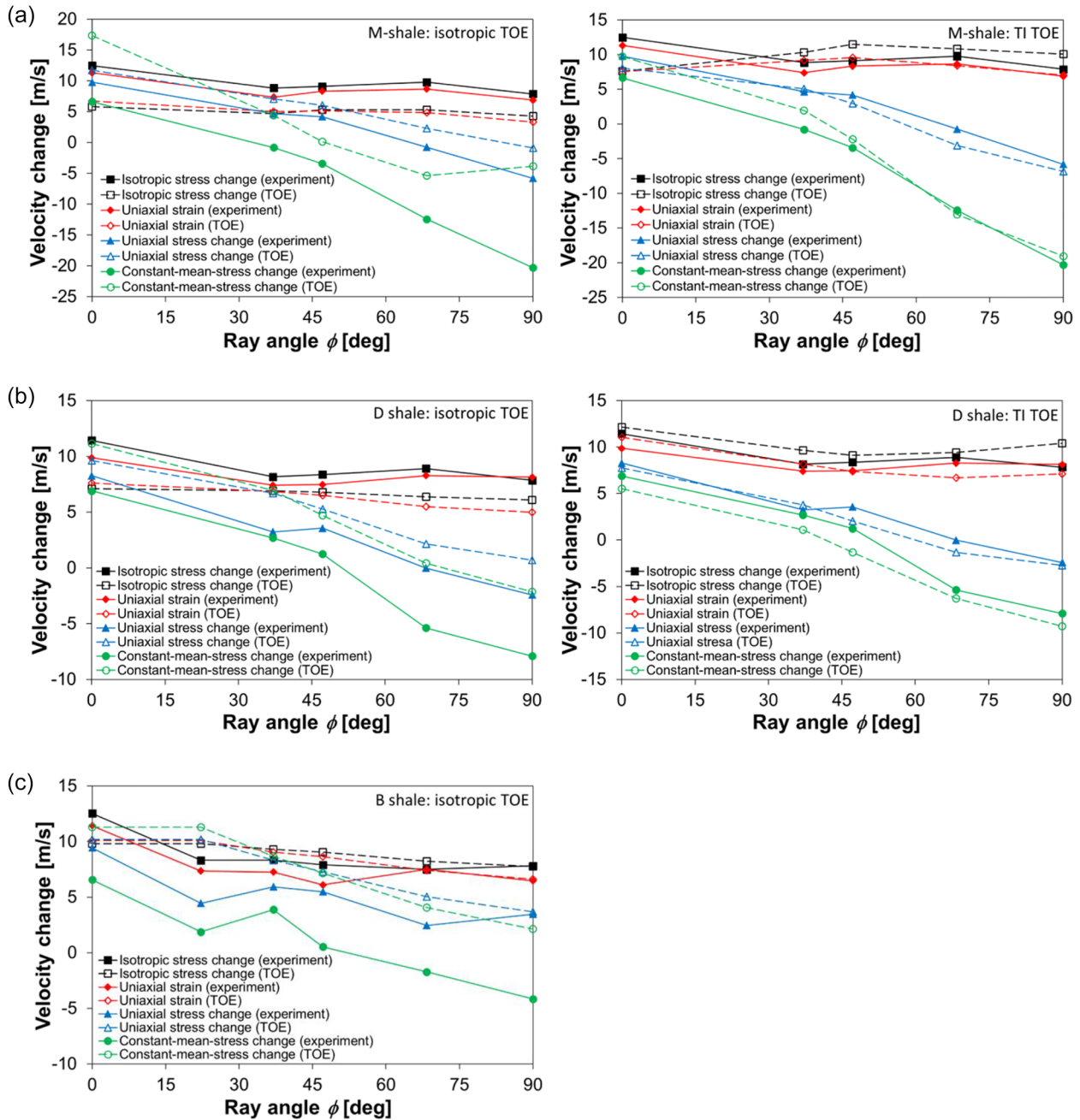


**FIGURE 7** Group velocity changes, for 5 MPa vertical loading, versus ray angle for the different stress paths for (a) M shale, (b) D shale and (c) B shale, with measured data (full connection lines) and predicted data by the isotropic and TI TOE models (broken connection lines), respectively. The 95% confidence interval for the measured data is  $\pm 5.6$  m/s. B shale was not calibrated to the TI TOE model because the vertical S-wave velocity changes were not reliable.

horizontal in-plane strains ( $e_1$ ) having qualitatively opposite sign to vertical strains (Figure 8). The horizontal tangential ('hoop') strains ( $e_2$ ) around the reservoir are positive due to the reservoir depletion. Generally, strain magnitude decreases with increasing static stiffness of the shales. With the axisymmetric model, the shear strains ( $e_3$ ) are anti-symmetric about the vertical symmetry axis of the reservoir. The presence of shear strain implies rotation of the corresponding prin-

cipal strain tensor relative to the coordinate system of the rock. Considering the vanishing strains outside the main strain cloud, the size of the geomechanical model is assessed to be sufficient to avoid adverse boundary effects.

Two-way traveltimes shifts were predicted as a function of angle with respect to the TI TOE model (not obtained for B shale) and the isotropic TOE model (Figure 9). With the TI TOE model, a pronounced peak of the traveltimes shifts is



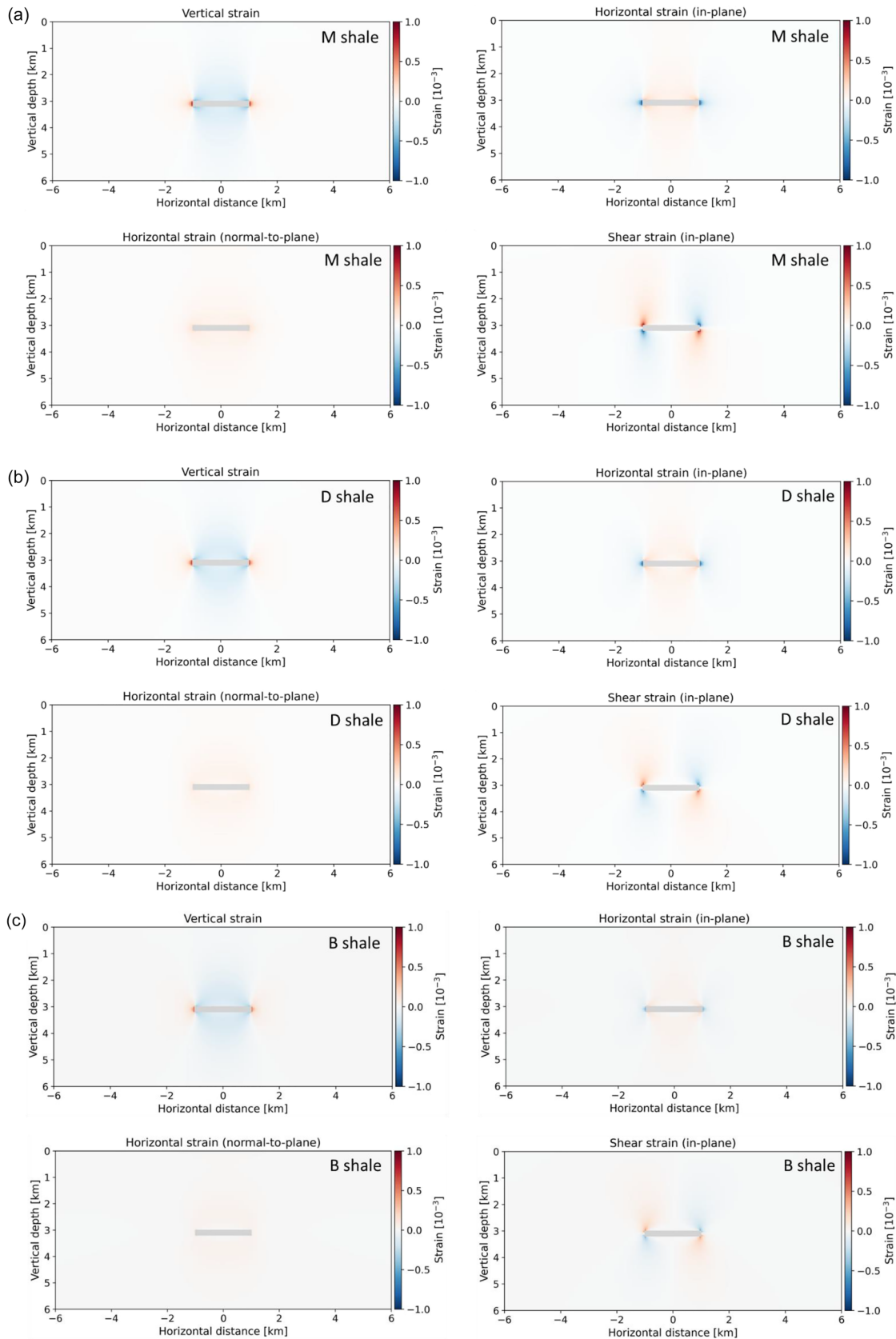


**FIGURE 8** Strains in the vertical section  $[x_1, x_3]$  obtained from the modelling case upon 35 MPa uniform reservoir depletion, with properties of the surrounding rocks equivalent to (a) M shale, (b) D shale and (c) B shale. Reservoir is indicated by the grey rectangle in the centre of the figures.

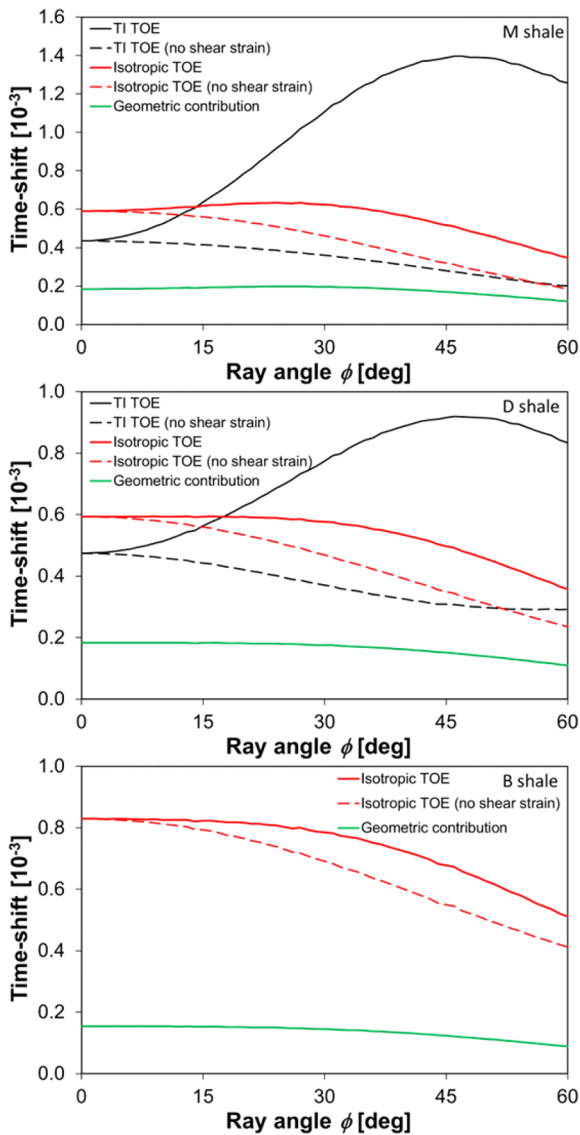


**FIGURE 9** Two-way traveltimes shifts for the modelling cases predicted by the TI TOE model (not obtained for B shale) and the isotropic TOE model. Two additional variants are included: one disregarding the shear strain ( $e_5 = 0$ ) in the TOE models and the other considering only the geometric contribution to the time-shift.

predicted at ray angles around  $45^\circ$ . In contrast, with the isotropic TOE model, the time-shifts are decreasing with increasing angle for D and B shales, whereas for M shale, the time-shifts reach a slight peak at  $20^\circ$ . Shear strains have a significant impact on time-shifts, especially in the TI TOE model. The geometric contribution to the time-shifts (Equation 43) is relatively small for all shales. The largest vertical time-shift is observed for B shale, primarily due to stress arching that increases with the stiffness of the non-reservoir formations (Mulders, 2003; Yan et al., 2020, 2023). To better visualize the spatial variation of the dynamic changes, time-

strains are provided at  $0^\circ$  and  $45^\circ$  (Figures 10 and 11), as further discussed below.

## DISCUSSION

We have developed a TOE tensor with TI symmetry, which satisfactorily predicts P-wave velocity changes measured in two overburden field shales covering a wide range of propagation directions and stress variations. The TI TOE model allows us to quantify the anisotropy of the strain sensitivity by analysing the dynamic response to a small uniaxial strain (0.001) applied along the horizontal ( $x_1$ ) and vertical ( $x_3$ ) directions, respectively. Consequently, the symmetry of the deformed medium, which possesses TI symmetry in the baseline state, maintains TI symmetry under uniaxial vertical strain while transforming to orthorhombic symmetry under uniaxial horizontal strain (Fuck & Tsvankin, 2009). In Figure 12, Thomsen's anisotropy parameters  $\epsilon_{Th}$ ,  $\delta_{Th}$  and  $\gamma_{Th}$  (Thomsen, 1986), extended to orthorhombic media by Tsvankin (1997), are quantified within the  $[x_1, x_3]$  plane for D shale. The horizontal strain sensitivity predicted by the TI TOE model significantly exceeds the vertical strain sensitivity for both  $\epsilon_{Th}$  and  $\delta_{Th}$ . In contrast, the isotropic TOE model predicts a notably smaller horizontal strain sensitivity for these parameters. For both TOE models,  $\gamma_{Th}$  demonstrates a relatively low strain sensitivity in both directions. It is also verified that, for small strains, the Thomsen parameters exhibit near perfect linear correlation with the uniaxial strain. B shale exhibits similar strain sensitivities as D shale with respect to the Thomsen parameters.

The calibration of the TOE coefficients seems robust, with the determined values closely aligning with the mean values obtained from the error analysis through random variations within their precision limits. This indicates a globally optimized set of TOE coefficients. For D shale, we bootstrapped the inversion of the TI TOE coefficients by using subsets of experimental data including only two stress paths, resulting in six subsets, as also discussed by Duda et al. (2020) with a hexagonal TOE model. Except for the subset that included the isotropic stress path and the uniaxial-strain path, all bootstrapped TOE coefficients remained within the 95% confidence interval obtained in the complete inversion. For M shale, only the isotropic stress path for  $C_{66}$  was used in the inversion of the TI TOE coefficients, which implied relatively large errors of  $C_{111}$  and  $C_{166}$ . The corresponding errors for D shale, utilizing four stress paths for  $C_{66}$  in the inversion, are significantly smaller. Including a diversity of stress paths in the calibration of the TOE coefficients seems thus to improve the quality and robustness of the predictions. Field-specific geomechanical modelling can be used to assess which stress

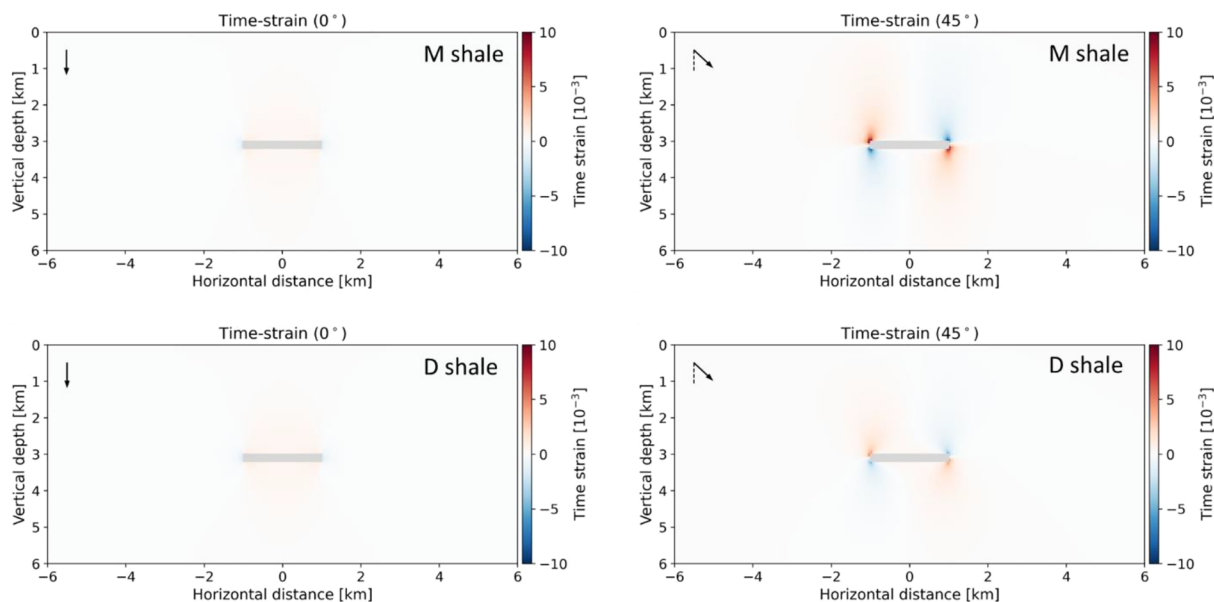


**FIGURE 10** Time-strains for the modelling case predicted by the TI TOE model for ray angles at 0° and 45°, where the directions are indicated with the inserted arrows.

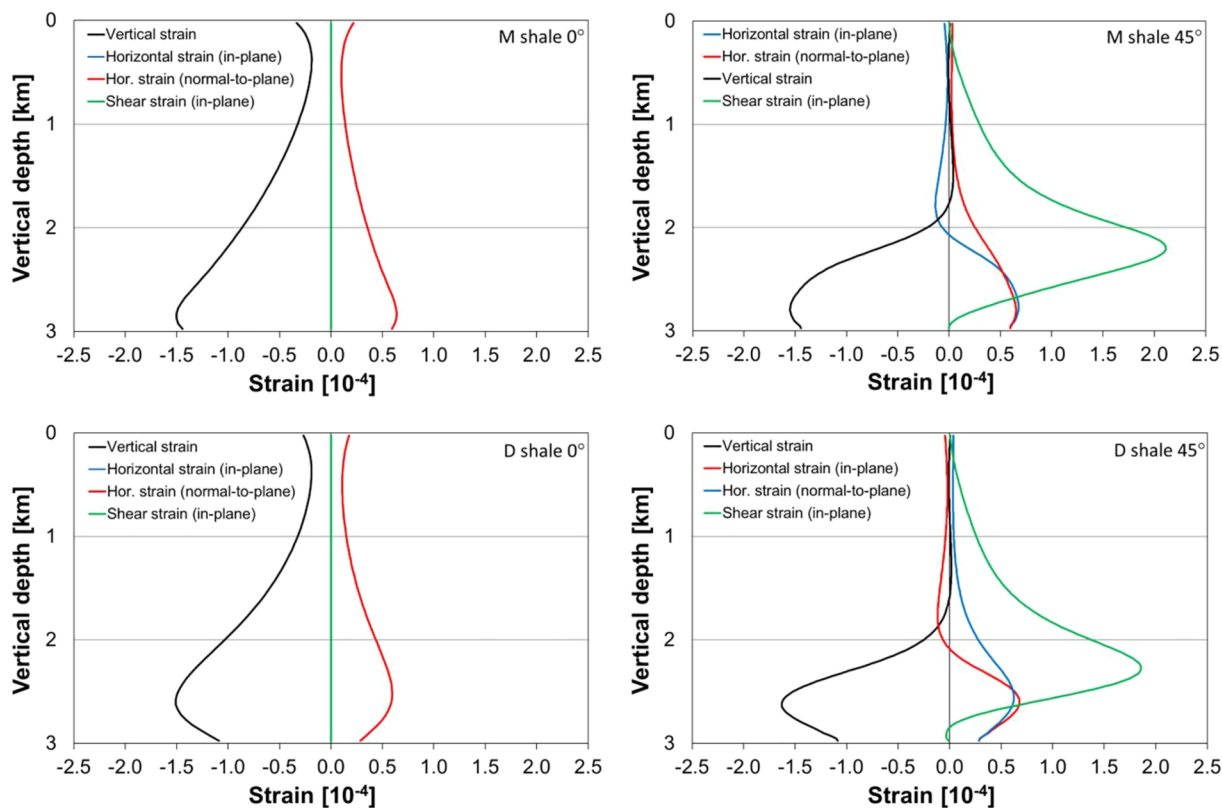


**FIGURE 11** Vertical strain ( $e_3$ ), horizontal in-plane strain ( $e_1$ ), horizontal normal-to-plane strain ( $e_2$ ) and in-plane shear strain ( $e_5$ ) as functions of depth obtained from the modelling with M and D shale properties, respectively. Data correspond to the straight ray path from the left source to the reflection point at 0° and 45° ray angles, respectively (Figure 6). The horizontal strains are equal at 0° ray angle due to the symmetry.

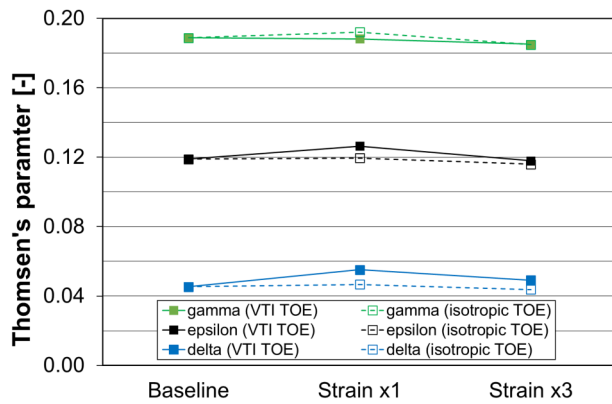


**FIGURE 12** Thomsen's anisotropy parameters for D shale in the baseline and monitor states upon a uniaxial (compacting) strain of magnitude 0.001 along the  $x_1$  (horizontal) and  $x_3$  (vertical) directions, predicted by the TI TOE model (full connection lines) and by the isotropic TOE model (broken connection lines).

paths are relevant from case to case (Mulders, 2003; Yan et al., 2023). In our study, two tests were needed to obtain all nine TI TOE coefficients, because the setup was limited to isotropic horizontal stresses. In a true-triaxial setup, stresses and strains can be individually adjusted in three orthogonal directions. A complete inversion of all TI TOE coefficients and a larger variation in stress paths can thus be obtained from a single test in a true-triaxial setup.

We advocate the importance of conducting undrained experiments on overburden shales. The strain sensitivity of dynamic stiffness in shale will generally be different in statically drained conditions as compared to undrained conditions (Bauer et al., 2008; Fjær, 2019; Holt et al., 2018). The monitoring of a producing field typically spans from months to a few decades. Shales, abundant in the overburden, are known for their low permeability. It is commonly assumed that shales exhibit undrained static stiffness (Bauer et al., 2008; Delle Piane et al., 2011; Islam & Skalle, 2013; MacBeth & Bachkheti, 2021; Sarout & Guéguen, 2008; Soldal et al., 2021; Thompson et al., 2021). In low-permeability formations, the immediate response to reservoir depletion is a heterogeneous undrained pore-pressure change that occurs within a substantial volume surrounding the reservoir, encompassing the entire overburden (Duda et al., 2023; Yan et al., 2023). The permeability and characteristic diffusion lengths can be used to estimate the time required for pore-pressure equilibration upon a strain in a low-permeable overburden, suggesting that an undrained overburden response during a field's lifespan is realistic, as discussed by Duda et al. (2023). Overpressured zones and hydrocarbon containment over geological time further support the presence of a low-permeable overburden that exhibits minimal drainage. However, drainage may effectively occur outside the reservoir in gas clouds and in areas with more permeable formations, such as in sandy

layers and fractured zones. Drainage may also take place in formations near the reservoir and wells implying short diffusion lengths, though permeability is also a determining factor. Nevertheless, a significant proportion of the overburden can reasonably be assumed to exhibit undrained static behaviour throughout the lifespan of a producing field, as reflected in our model. In zones more prone to drainage, an assessment of pore-pressure equilibration is necessary to determine whether a drained TOE model is needed. A drained TOE model is expected to be more complex than the TOE model described here because an explicit inclusion of the pore-pressure dependence is required. To calibrate a drained TI TOE model for overburden shales, laboratory tests conducted under drained conditions are necessary. The undrained tests we performed took 2–4 weeks per test, and it is anticipated that similar tests under drained conditions will require 4–8 weeks per test due to the extremely low permeability. Notably, the isotropic TOE coefficients obtained by Prioul et al. (2004) and Prioul and Lebrat (2004) were obtained from drained tests (MacBeth & Bachkheti, 2021). Hornby (1998) and Bathija et al. (2009) showed that the strain sensitivity of velocities may be very different at low total stress as compared to high total stress. This underlines the importance of testing the rocks as close as possible to relevant (in situ) stress, pore-pressure and drainage conditions.

Ultrasonic velocities in the laboratory are typically recorded in the 0.1–1 MHz range, whereas seismic data effectively cover the 1–100 Hz range (Batzle et al., 2006; Delle Piane et al., 2014; Duranti et al., 2005; Lozovyi & Bauer, 2019; Szweczyk et al., 2018). Laboratory measurements of Mancos outcrop shale indicate a higher stress sensitivity at seismic frequencies than at ultrasonic frequencies (Lozovyi, 2018; Szweczyk et al., 2018). At present, ultrasonic tests quantifying strain- and stress-sensitivities offer significantly higher accuracy and more flexibility as compared to low-frequency tests, so we have used the ultrasonic data without modification.

The geomechanical modelling demonstrates a significant impact of shear-strain magnitude on the angular time-shift trend predicted by the TI TOE model, exhibiting a maximum at offset angles around  $45^\circ$  (Figure 9). This is consistent with vanishing shear strains along the  $0^\circ$  ray path, and significant shear-strains along the  $45^\circ$  ray path for which the shear strain peaks at a depth level 700–800 m above the reservoir (Figures 10 and 11). In our axisymmetric case,  $e_5$  is the only nonzero shear strain. Thus, the shear-strain contribution to the monitor stiffness is only associated with the TOE coefficients  $C_{144}$ ,  $C_{344}$  and  $C_{456}$  (Equation 13). However, compared to the TI TOE model, these coefficients are relatively small in the isotropic TOE model (Table 4), which may explain the relatively low sensitivity to shear strains in the time-shifts predicted by the isotropic TOE model (Figure 9).

Various offset-trends of time-shifts are reported by MacBeth et al. (2018). However, these field cases are very different regarding location, processing and analysis. For an idealized isotropic medium with no lateral variations in stiffness, strain and velocity changes, and isotropic velocity changes, the time-strain in a vertically stretching formation decreases with increasing angle prior to normal moveout correction, whereas it increases after normal moveout correction (Bakk, Holt, Bauer, et al., 2020; Landrø & Janssen, 2002; Landrø & Stammeijer, 2004). This illustrates the importance of comparing 4D attributes within the same context, that is whether it is pre-stack or post-stack data. Even though post-stack analysis of 4D data in many cases gives substantial insight into production-induced events, pre-stack analysis may disclose details that would be difficult to observe in stacked data (Dvorak et al., 2018; Evensen & Landrø, 2010; Røste et al., 2007; Shragge & Lumley, 2013).

In addition to the synthetic cases addressed in this study, it is important to discuss the feasibility and applicability of our model and method for improving field data processing. Our work highlights the importance of integrating 4D seismic analysis, geomechanical modelling and TOE models to improve quantification of strains. A potential avenue for field applications involves leveraging the significant dependency of dynamic changes on stress path and ray angle (Figure 7) to quantify the magnitude and direction of strains and stress changes. This could be achieved by inverting 4D seismic time-shifts using the anisotropic TOE model, or a simplified version, in conjunction with geomechanical modelling data. To explicitly address the spatial and angular velocity dependencies associated with mechanical changes, the application of 4D tomography may be a suitable method for analysing pre-stack seismic data (e.g. Dvorak et al., 2018; Evensen & Landrø, 2010). This approach can facilitate a more comprehensive understanding of the important interplay between mechanical alterations and the spatial and angular dependencies of velocity changes. Since the TI TOE model seems to be sensitive to shear strains, such a model may be used to detect shear-zones of importance for rock integrity, well stability and infill drilling.

Although the TI TOE model predicts the experimental data well, nine TOE coefficients need to be determined. To make such models more applicable, correlations between the coefficients or a reduction of independent coefficients would be beneficial. More laboratory testing, better utilization of existing data and a sensitivity analysis of the model will be important. Further progress could also be achieved by comparing TOE models to micromechanical models to obtain a more intuitive understanding of the underlying physics (Sripanich et al., 2021).

## SUMMARY AND CONCLUSIONS

A strain-dependent TOE tensor with TI symmetry has been developed. Both the TI model and the analogue model with isotropic TOE tensor were calibrated using velocity changes from laboratory tests on field shales. The TI TOE model adequately predicted the P-wave velocity data obtained across a large span of stress paths and propagation angles in the experiments. Although the isotropic TOE model captured the angular trends of velocity changes satisfactorily, it exhibited some quantitative misfit depending on the stress path. Based on strains obtained from a modelling case with a depleting reservoir surrounded by shales, overburden time-shifts were predicted as a function of angle using both TOE models. The isotropic TOE model significantly underestimated the time-shifts at higher angles, as compared to the TI TOE model, mainly attributed to low sensitivity to shear strains in the isotropic TOE model. This study highlights the potential of pre-stack time-lapse data analysis for improving the detection of altered stresses and strains, which may not be evident from post-stack data. It also emphasizes the importance of interaction among the geophysics, geomechanics and rock physics disciplines for a better understanding of static and dynamic alterations in the subsurface.

## ACKNOWLEDGEMENTS


This work received support from the Research Council of Norway, through grants 234074 and 294369 in PETROMAKS 2, AkerBP, Equinor, Shell Global Solutions B.V., Vår Energi, INEOS Energy, and TotalEnergies. Special thanks to Eyvind F. Sønstebø for conducting several of the tests at SINTEF Formation Physics Laboratory and Andreas Bauer for contributing to the laboratory data analysis. We also thank Idar Larsen, Lang Liu, Arne Marius Raaen and Erling Fjær for their contributions.

## DATA AVAILABILITY STATEMENT


Restrictions apply to the availability of these data that support the results of this study, which were generated under the projects *Improved prediction of stress and pore-pressure changes in the overburden for infill drilling* and *Shale Rock Physics: Improved Seismic Monitoring for Increased Recovery*. Data are available from SINTEF AS, by its research institute SINTEF Industry, subject to the permissions of the owners of the data.




## ORCID

Audun Bakk  <https://orcid.org/0000-0003-0581-6909>

Marcin Duda  <https://orcid.org/0000-0002-9916-0199>

Xiyang Xie  <https://orcid.org/0000-0001-8205-9126>

Jørn F. Stenebråten  <https://orcid.org/0000-0002-9702-6850>

Hong Yan  <https://orcid.org/0000-0002-3941-8047>  
 Colin MacBeth  <https://orcid.org/0000-0001-8593-3456>  
 Rune M. Holt  <https://orcid.org/0000-0003-1763-7836>

## REFERENCES

- Angus, D.A., Dutko, M., Kristiansen, T.G., Fisher, Q.J., Kendall, J.-M., Baird, A.F. et al. (2015) Integrated hydro-mechanical and seismic modelling of the Valhall reservoir: a case study of predicting subsidence, AVOA and microseismicity. *Geomechanics for Energy and the Environment*, 2, 32–44. <https://doi.org/10.1016/j.gete.2015.05.002>
- Asaka, M. (2023) Anisotropic 4D seismic response inferred from ultrasonic laboratory measurements: a direct comparison with the isotropic response. *Geophysical Prospecting*, 71, 17–28. <https://doi.org/10.1111/1365-2478.13273>
- Bakk, A., Holt, R.M., Bauer, A., Dupuy, B. & Romdhane, A. (2020) Offset dependence of overburden time-shifts from ultrasonic data. *Geophysical Prospecting*, 68, 1847–1863. <https://doi.org/10.1111/1365-2478.12963>
- Bakk, A., Holt, R.M., Duda, M. & MacBeth, C. (2020). The fate of R in light of field shale laboratory tests [Conference proceedings]. *EAGE 2020 Conference Online*. EAGE. pp. 1–5. <https://doi.org/10.3997/2214-4609.202011500>
- Barkved, O.I., Kristiansen, T. & Fjær, E. (2005) The 4D seismic response of a compacting reservoir – examples from the Valhall Field, Norway [Expanded abstracts]. *75th SEG Annual Meeting*. Houston, TX, USA. SEG. pp. 2508–2511. <https://doi.org/10.1190/1.2148232>
- Bathija, A.P., Batzle, M.L. & Prasad, M. (2009) An experimental study of the dilation factor. *Geophysics*, 74, E181–E191. <https://library.seg.org/doi/abs/10.1190/1.3137060>
- Batzle, M.L., Han, D.-H. & Hofmann, R. (2006) Fluid mobility and frequency-dependent seismic velocity—direct measurements. *Geophysics*, 71, N1–N9. <https://library.seg.org/doi/10.1190/1.2159053>
- Bauer, A., Lehr, C., Korndorffer, F., van der Linden, A., Dudley, J., Addis, T. et al. (2008) Stress and pore-pressure dependence of sound velocities in shales: poroelastic effects in time-lapse seismic [Expanded abstracts]. *78th SEG Annual Meeting*. Las Vegas, NV, USA. SEG. pp. 1630–1634. <https://doi.org/10.1190/1.3059221>
- Berryman, J.G. (1979) Long-wave elastic anisotropy in transversely isotropic media. *Geophysics*, 44, 896–917. <https://doi.org/10.1190/1.1440984>
- Birch, F. (1947) Finite elastic strain of cubic crystals. *Physical Review*, 71, 809–824. <https://doi.org/10.1103/PhysRev.71.809>
- Brugger, K. (1964) Thermodynamic definition of higher order coefficients. *Physical Review*, 133, A1611–A1612. <https://doi.org/10.1103/PhysRev.133.A1611>
- Brugger, K. (1965) Pure modes for elastic waves in crystals. *Journal of Applied Physics*, 36, 759–768. <https://doi.org/10.1063/1.1714215>
- Cheng, A.H.-D. (1997) Material coefficients of anisotropic poroelasticity. *International Journal of Rock Mechanics and Mining Sciences*, 34, 199–205. [https://doi.org/10.1016/S0148-9062\(96\)00055-1](https://doi.org/10.1016/S0148-9062(96)00055-1)
- Crampin, S., Chesnokov, E.M. & Hipkin, R.G. (1984) Seismic anisotropy—the state of the art: II. *Geophysical Journal International*, 76, 1–16. <https://doi.org/10.1111/j.1365-246X.1984.tb05017.x>
- De Gennaro, S., Onaisi, A., Grandi, A., Ben-Brahim, L. & Neillo, V. (2008) 4D reservoir geomechanics: a case study from the HP/HT reservoirs of the Elgin and Franklin fields. *First Break*, 26, 53–59. <https://doi.org/10.3997/1365-2397.2008019>
- Delle Piane, C., Dewhurst, D.N., Siggins, A.F. & Raven, M.D. (2011) Stress-induced anisotropy in brine saturated shale. *Geophysical Journal International*, 184, 897–906. <https://doi.org/10.1111/j.1365-246X.2010.04885.x>
- Delle Piane, C., Sarout, J., Madonna, C., Saenger, E.H., Dewhurst, D.N. & Raven, M. (2014) Frequency-dependent seismic attenuation in shales: experimental results and theoretical analysis. *Geophysical Journal International*, 198, 504–515. <https://doi.org/10.1093/gji/ggu148>
- Dellinger, J. & Vernik, L. (1994) Do traveltimes in pulse-transmission experiments yield anisotropic group or phase velocities? *Geophysics*, 59, 1774–1779. <https://doi.org/10.1190/1.1443564>
- Dewhurst, D.N. & Siggins, A.F. (2006) Impact of fabric, microcracks and stress field on shale anisotropy. *Geophysical Journal International*, 165, 135–148. <https://doi.org/10.1111/j.1365-246X.2006.02834.x>
- Ditlevsen, F., Bourgeois, F. & Calvert, M. (2018) Handling wellbore instability in overburden Tertiary shales [Conference proceedings]. *80th EAGE Conference & Exhibition*. Copenhagen, Denmark. EAGE. pp. 1–5. <https://doi.org/10.3997/2214-4609.201800721>
- Donald, J.A. & Prioul, R. (2015) In situ calibrated velocity-to-stress transforms using shear sonic radial profiles for time-lapse production analysis. *The Leading Edge*, 34, 286–294. <https://doi.org/10.1190/tle34030286.1>
- Duda, M.I., Bakk, A., Holt, R.M. & Stenebråten, J.F. (2023) Anisotropic poroelastic modelling of depletion-induced pore pressure changes in Valhall overburden. *Rock Mechanics and Rock Engineering*, 56, 3115–3137. <https://doi.org/10.1007/s00603-022-03192-0>
- Duda, M.I., Holt, R.M. & Bakk, A. (2020) Third-order elastic tensor of shales determined through ultrasonic velocity measurements [Conference proceedings]. *54th US Rock Mechanics/Geomechanics Symposium*. ARMA-2020-1237. <https://onepetro.org/ARMAUSRMS/proceedings/ARMA20/All-ARMA20/ARMA-2020-1237/447487>
- Dudley, J.W., Brignoli, M., Crawford, B.R., Ewy, R.T., Love, D.K., McLennan, J.D. et al. (2016) ISRM suggested method for uniaxial-strain compressibility testing for reservoir geomechanics. *Rock Mechanics and Rock Engineering*, 49, 4153–4178. <https://doi.org/10.1007/s00603-016-1055-4>
- Duranti, L., Ewy, R. & Hofmann, R. (2005) Dispersive and attenuative nature of shales: multiscale and multifrequency observations [Expanded abstracts]. *75th SEG Annual Meeting*. Houston, TX, USA. SEG. pp. 1577–1580. <https://doi.org/10.1190/1.2147994>
- Dvorak, I., MacBeth, C. & Amini, H. (2018) Evaluating 4D overburden velocity perturbation for the Shearwater field via pre-stack time-shift inversion [Conference proceedings]. *80th EAGE Conference & Exhibition*. Copenhagen, Denmark. EAGE. pp. 1–5. <https://doi.org/10.3997/2214-4609.201800699>
- Evensen, A.K. & Landrø, M. (2010) Time-lapse tomographic inversion using a Gaussian parameterization of the velocity changes. *Geophysics*, 75, U29–U38. <https://library.seg.org/doi/10.1190/1.3442573>
- Ewy, R.T. (2021) Well shear associated with conventional and unconventional operations: diagnosis and mechanisms. *SPE Drilling & Completion*, 36, 427–444. <https://doi.org/10.2118/205007-PA>
- Fedorov, F.I. (1968) *Theory of elastic waves in crystals*. New York: Springer. <https://link.springer.com/book/10.1007/978-1-4757-1275-9>
- Fjær, E. (2019) Relations between static and dynamic moduli of sedimentary rocks. *Geophysical Prospecting*, 67, 128–139. <https://doi.org/10.1111/1365-2478.12711>

- Fjær, E., Holt, R.M., Horsrud, P. & Raaen, A.M. (2021) *Petroleum related rock mechanics*, 3rd edition. Amsterdam: Elsevier Science. <https://www.elsevier.com/books/petroleum-related-rock-mechanics/fjaer/978-0-12-822195-2>
- Fuck, R.F., Bakulin, A. & Tsvankin, I. (2009) Theory of traveltimes shifts around compacting reservoirs: 3D solutions for heterogeneous anisotropic media. *Geophysics*, 74, D25–D36. <https://library.seg.org/doi/abs/10.1190/1.3033215>
- Fuck, R.F. & Tsvankin, I. (2009) Analysis of the symmetry of a stressed medium using nonlinear elasticity. *Geophysics*, 74, WB79–WB87. <https://library.seg.org/doi/10.1190/1.3157251>
- Fumi, F.G. (1951) Third-order elastic coefficients of crystals. *Physical Review*, 83, 1274–1275. <https://doi.org/10.1103/PhysRev.83.1274>
- Fumi, F.G. (1952) Third-order elastic coefficients in trigonal and hexagonal crystals. *Physical Review*, 86, 561. <https://doi.org/10.1103/PhysRev.86.561>
- Geertsma, J. (1973) Land subsidence above compacting oil and gas reservoirs. *Journal of Petroleum Technology*, 25, 734–744. <https://doi.org/10.2118/3730-PA>
- Guilbot, J. & Smith, B. (2002) 4-D constrained depth conversion for reservoir compaction estimation: application to Ekofisk field. *The Leading Edge*, 21, 302–308. <https://doi.org/10.1190/1.1463782>
- Hall, S.A., MacBeth, C., Barkved, O.I. & Wild, P. (2002) Time-lapse seismic monitoring of compaction and subsidence at Valhall through cross-matching and interpreted warping of 3D streamer and OBC data [Expanded abstracts]. 72nd SEG Annual Meeting. Salt Lake City, UT, USA. SEG. pp. 1696–1699. <https://doi.org/10.1190/1.1817004>
- Hatchell, P. & Bourne, S. (2005) Rocks under strain: strain-induced time-lapse time shifts are observed for depleting reservoirs. *The Leading Edge*, 24, 1222–1225. <https://library.seg.org/doi/abs/10.1190/1.2149624>
- Hawkins, K. (2008) Defining the extent of the compacting Elgin reservoir by measuring stress-induced anisotropy. *First Break*, 26, 81–88. <https://doi.org/10.3997/1365-2397.26.10.28559>
- Hearmon, R.F.S. (1953) ‘Third-order’ elastic coefficients. *Acta Crystallographica*, 6, 331–340. <https://doi.org/10.1107/S0365110x53000909>
- Helbig, K. & Thomsen, L. (2005) 75-plus years of anisotropy in exploration and reservoir seismics: a historical review of concepts and methods. *Geophysics*, 70, 9ND–23ND. <https://doi.org/10.1190/1.2122407>
- Herwanger, J.V. & Horne, S.A. (2009) Linking reservoir geomechanics and time-lapse seismics: predicting anisotropic velocity changes and seismic attributes. *Geophysics*, 74, W13–W33. <https://library.seg.org/doi/abs/10.1190/1.3122407>
- Herwanger, J. & Koutsabeloulis, N. (2011). *Seismic geomechanics: how to build and calibrate geomechanical models using 3D and 4D seismic data*. Utrecht, The Netherlands; EAGE Publications.
- Hodgson, N. (2009) *Inversion for reservoir pressure change using overburden strain measurements determined from 4D seismic* (PhD thesis). Scotland, UK: Heriot-Watt University. <https://www.ros.hw.ac.uk/handle/10399/2320>
- Holt, R.M., Bauer, A. & Bakk, A. (2018) Stress-path-dependent velocities in shales: impact on 4D seismic interpretation. *Geophysics*, 83, MR353–MR367. <https://doi.org/10.1190/geo2017-0652.1>
- Hornby, B.E. (1998) Experimental laboratory determination of the dynamic elastic properties of wet, drained shales. *Journal of Geophysical Research: Solid Earth*, 103, 29945–29964. <https://doi.org/10.1029/97JB02380>
- Hudson, J.A. (1981) Wave speeds and attenuation of elastic waves in material containing cracks. *Geophysical Journal International*, 64, 133–150. <https://doi.org/10.1111/j.1365-246X.1981.tb02662.x>
- Hughes, D.S. & Kelly, J.L. (1953) Second-order elastic deformation of solids. *Physical Review*, 92, 1145–1149. <https://doi.org/10.1103/PhysRev.92.1145>
- Islam, M.A. & Skalle, P. (2013) An experimental investigation of shale mechanical properties through drained and undrained test mechanisms. *Rock Mechanics and Rock Engineering*, 46, 1391–1413. <https://doi.org/10.1007/s00603-013-0377-8>
- Jaeken, J.W. & Cottenier, S. (2016) Solving the Christoffel equation: phase and group velocities. *Computer Physics Communications*, 207, 445–451. <https://doi.org/10.1016/j.cpc.2016.06.014>
- Johnston, D.H. (1987) Physical properties of shale at temperature and pressure. *Geophysics*, 52, 1391–1401. <https://doi.org/10.1190/1.1442251>
- Jones, L.E.A. & Wang, H.F. (1981) Ultrasonic velocities in Cretaceous shales from the Williston basin. *Geophysics*, 46, 288–297. <https://doi.org/10.1190/1.1441199>
- Kenter, C.J., Van den Beukel, A.C., Hatchell, P.J., Maron, K.P., Molenaar, M.M. & Stammeijer, J.G.F. (2004) Geomechanics and 4D: evaluation of reservoir characteristics from timeshifts in the overburden. *Gulf Rocks 2004; 6th North America Rock Mechanics Symposium (NARMS), Houston, TX, USA*. ARMA-04-627. <https://onepetro.org/ARMANARMS/proceedings-abstract/ARMA04/All-ARMA04/ARMA-04-627/117669>
- Kristiansen, T.G., Barkved, O.I., Buer, K. & Bakke, R. (2005) Production-induced deformations outside the reservoir and their impact on 4D seismic [Conference proceedings]. *International Petroleum Technology Conference, Doha, Qatar*. pp. 1–12. <https://onepetro.org/IPTCONF/proceedings-abstract/05IPTC/All-05IPTC/IPTC-10818-MS/30437>
- Kudarova, A., Hatchell, P., Brain, J. & MacBeth, C. (2016) Offset-dependence of production-related 4D time-shifts: real data examples and modelling [Expanded abstracts]. *86th SEG Annual Meeting*. Dallas, TX, USA. SEG. pp. 5395–5399. <https://doi.org/10.1190/segam2016-13611549.1>
- Landrø, M. & Janssen, R. (2002) Estimating compaction and velocity changes from time-lapse near and far offset stacks [Conference proceedings]. *64th EAGE Conference & Exhibition*. Florence, Italy. EAGE. P036. <https://doi.org/10.3997/2214-4609-pdb.5.P036>
- Landrø, M. & Stammeijer, J. (2004) Quantitative estimation of compaction and velocity changes using 4D impedance and traveltimes changes. *Geophysics*, 69, 949–957. <https://library.seg.org/doi/10.1190/1.1778238>
- Larsen, I., Stenebråten, J.F. & Bakk, A. (2011) Stress dependent dynamic anisotropy in shales [Conference abstracts]. *9th Euroconference on Rock Physics and Geomechanics, Trondheim, Norway*. <https://www.ntnu.edu/euroconference-2011/program>
- Lozovyi, S. (2018) *Seismic dispersion and the relation between static and dynamic stiffness of shales* (PhD Thesis). Norway: Norwegian University of Science and Technology. <https://ntnuopen.ntnu.no/ntnu-xmlui/handle/11250/2564704>
- Lozovyi, S. & Bauer, A. (2019) Velocity dispersion in rocks: a laboratory technique for direct measurement of P-wave modulus at seismic frequencies. *Review of Scientific Instruments*, 90, 024501. <https://doi.org/10.1063/1.5026969>
- Lubarda, V.A. (1997) New estimates of the third-order elastic constants for isotropic aggregates of cubic crystals. *Journal of the Mechanics*

- and *Physics of Solids*, 45, 471–490. [https://doi.org/10.1016/S0022-5096\(96\)00113-5](https://doi.org/10.1016/S0022-5096(96)00113-5)
- MacBeth, C. & Bachkheta, S. (2021) A geomechanical correction for time-lapse amplitude variation with offset. *Geophysics*, 86, M29–M40. <https://library.seg.org/doi/10.1190/geo2020-0398.1>
- MacBeth, C., Kudarova, A. & Hatchell, P. (2018) Review paper: a semi-empirical model of strain sensitivity for 4D seismic interpretation. *Geophysical Prospecting*, 66, 1327–1348. <https://doi.org/10.1111/1365-2478.12648>
- Mah, M. & Schmitt, D.R. (2003) Determination of the complete elastic stiffnesses from ultrasonic phase velocity measurements. *Journal of Geophysical Research: Solid Earth*, 108, ECV 6-1–ECV 6-11. <https://doi.org/10.1029/2001JB001586>
- Mavko, G., Mukerji, T. & Godfrey, N. (1995) Predicting stress-induced velocity anisotropy in rocks. *Geophysics*, 60, 1081–1087. <https://library.seg.org/doi/10.1190/1.1443836>
- Mulders, F.M.M. (2003) *Modelling of stress development and fault slip in and around a producing gas reservoir* (PhD Thesis). Delft, The Netherlands: Delft University of Technology. <https://repository.tudelft.nl/islandora/object/uuid%3Abe742135-10d7-4d69-bdee-f808b5926065>
- Nye, J.F. (1985) *Physical properties of crystals: their representation by tensors and matrices*. Oxford: Oxford University Press. <https://global.oup.com/academic/product/physical-properties-of-crystals-9780198511656>
- Pervukhina, M., Dewhurst, D., Gurevich, B., Kuila, U., Siggins, T., Raven, M. et al (2008) Stress-dependent elastic properties of shales: measurement and modelling. *The Leading Edge*, 27, 772–779. <https://library.seg.org/doi/10.1190/1.2944162>
- Prioul, R., Bakulin, A. & Bakulin, V. (2004) Nonlinear rock physics model for estimation of 3D subsurface stress in anisotropic formations: theory and laboratory verification. *Geophysics*, 69, 415–425. <https://library.seg.org/doi/10.1190/1.1707061>
- Prioul, R. & Lebrat, T. (2004) Calibration of velocity-stress relationships under hydrostatic stress for their use under non-hydrostatic stress conditions [Expanded abstracts]. *74th SEG Annual Meeting*. Denver, CO, USA. SEG. pp. 1698–1701. <https://library.seg.org/doi/10.1190/1.1851153>
- Rasolofosaon, P. (1998) Stress-induced seismic anisotropy revisited. *Oil & Gas Science and Technology – Revue d'IFP Energies Nouvelles*, 53, 679–692. <https://doi.org/10.2516/ogst:1998061>
- Rickett, J., Duranti, L., Hudson, T., Regel, B. & Hodgson, N. (2007) 4D time strain and the seismic signature of geomechanical compaction at Genesis. *The Leading Edge*, 26, 644–647. <https://doi.org/10.1190/1.2737103>
- Røste, T. & Ke, G. (2017) Overburden 4D time shifts—indicating undrained areas and fault transmissibility in the reservoir. *The Leading Edge*, 36, 423–430. <https://library.seg.org/doi/10.1190/tle36050423.1>
- Røste, T., Landrø, M. & Hatchell, P. (2007) Monitoring overburden layer changes and fault movements from time-lapse seismic data on the Valhall Field. *Geophysical Journal International*, 170, 1100–1118. <https://doi.org/10.1111/j.1365-246X.2007.03369.x>
- Røste, T., Stovas, A. & Landrø, M. (2006) Estimation of layer thickness and velocity changes using 4D prestack seismic data. *Geophysics*, 71, S201–S234. <https://library.seg.org/doi/abs/10.1190/1.2335657>
- Sarkar, D., Bakulin, A. & Kranz, R.L. (2003) Anisotropic inversion of seismic data for stressed media: theory and a physical modelling study on Berea Sandstone. *Geophysics*, 68, 690–704. <https://doi.org/10.1190/1.1567240>
- Sarout, J. & Guéguen, Y. (2008) Anisotropy of elastic wave velocities in deformed shales: Part 1—Experimental results. *Geophysics*, 73, D75–D89. <https://library.seg.org/doi/10.1190/1.2952744>
- Sayers, C. M. & Kachanov, M. (1995) Microcrack-induced elastic wave anisotropy of brittle rocks. *Journal of Geophysical Research: Solid Earth*, 100, 4149–4156. <https://doi.org/10.1029/94JB03134>
- Scott, T.E. (2007) The effects of stress paths on acoustic velocities and 4D seismic imaging. *The Leading Edge*, 26, 602–608. <https://library.seg.org/doi/10.1190/1.2737101>
- Shapiro, S.A. (2017) Stress impact on elastic anisotropy of triclinic porous and fractured rocks. *Journal of Geophysical Research: Solid Earth*, 122, 2034–2053. <https://doi.org/10.1002/2016JB013378>
- Shragge, J. & Lumley, D. (2013) Time-lapse wave-equation migration velocity analysis. *Geophysics*, 78, S69–S79. <https://library.seg.org/doi/abs/10.1190/geo2012-0182.1>
- Sinha, B.K., (1982) Elastic waves in crystals under a bias. *Ferroelectrics*, 41, 61–73. <https://doi.org/10.1080/00150198208210610>
- Sinha, B.K. & Kostek, S. (1996) Stress-induced azimuthal anisotropy in borehole flexural waves. *Geophysics*, 61, 1899–1907. <https://library.seg.org/doi/10.1190/1.1444105>
- Skempton, A.W. (1954). The Pore-Pressure Coefficients A and B. *Géotechnique*, 4, 143–147. <https://doi.org/10.1680/geot.1954.4.4.143>
- Soldal, M., Skurtveit, E. & Choi, J.C. (2021) Laboratory evaluation of mechanical properties of Draupne shale relevant for CO<sub>2</sub> seal integrity. *Geosciences*, 11, 244. <https://doi.org/10.3390/geosciences11060244>
- Sripanich, Y., Vasconcelos, I., Tromp, J. & Trampert, J. (2021) Stress-dependent elasticity and wave propagation—new insights and connections. *Geophysics*, 86, W47–W64. <https://library.seg.org/doi/10.1190/geo2020-0252.1>
- Szewczyk, D., Bauer, A. & Holt, R.M. (2018) Stress-dependent elastic properties of shales—laboratory experiments at seismic and ultrasonic frequencies. *Geophysical Journal International*, 212, 189–210. <https://doi.org/10.1093/gji/ggx392>
- Thompson, N., Andrews, J.S. & Bjørnarå, T.I. (2021) Assessing potential thermo-mechanical impacts on caprock due to CO<sub>2</sub> injection—a case study from Northern Lights CCS. *Energies*, 14, 5054. <https://doi.org/10.3390/en14165054>
- Thomsen, L. (1986) Weak elastic anisotropy. *Geophysics*, 51, 1954–1966. <https://library.seg.org/doi/10.1190/1.1442051>
- Thurston, R.N. (1974) Waves in solids. In: Truesdell, C. (Ed.) *Mechanics of solids*. In: Flügge, S. (Ed.) *Encyclopedia of physics*, vol. VI4a. Berlin: Springer-Verlag, pp. 109–308. <https://link.springer.com/book/9783540131632>
- Thurston, R.N. & Brugger, K. (1964) Third-order elastic constants and the velocity of small amplitude elastic waves in homogeneously stressed media. *Physical Review*, 133, A1604–A1610. <https://doi.org/10.1103/PhysRev.133.A1604>
- Tsvankin, I. (1997) Anisotropic parameters and P-wave velocity for orthorhombic media. *Geophysics*, 62, 1292–1309. <https://doi.org/10.1190/1.1444231>
- Vernay, M., Morvan, M. & Breul, P. (2019) Evaluation of the degree of saturation using Skempton coefficient B. *Geomechanics and Geoengineering*, 15, 79–89. <https://doi.org/10.1080/17486025.2019.1620349>
- Wang, H. & Li, M. (2009) Ab initio calculations of second-, third-, and fourth-order elastic constants for single crystals. *Physical Review B*, 79, 224102. <https://doi.org/10.1103/PhysRevB.79.224102>
- Wang, W. & Schmitt, D.R. (2021) Static measurements of the third-order elastic constants of rocks [Conference proceedings].



- 55th US Rock Mechanics/Geomechanics Symposium. ARMA-2021-1189. <https://onepetro.org/ARMAUSRMS/proceedings-abstract/ARMA21/All-ARMA21/ARMA-2021-1189/467941>
- Winkler, K.W. & Liu, X. (1996) Measurements of third-order elastic constants in rocks. *Journal of the Acoustical Society of America*, 100, 1392–1397. <https://doi.org/10.1121/1.415986>
- Zoback, M.D. & Zinke, J.C. (2002) Production-induced normal faulting in the Valhall and Ekofisk oil fields. *Pure & Applied Geophysics*, 159, 403–420. <https://doi.org/10.1007/PL00001258>
- Yan, H., Bakk, A., Duda, M., Holt, R.M. & Lozovyi, S. (2023) Overburden 4D seismic analysis: influence of stress and pore-pressure changes accounting for elastic contrast between a reservoir and its anisotropic surrounding rocks. *Geophysics*, 88, 1–14. <https://doi.org/10.1190/geo2022-0033.1>
- Yan, H., Bakk, A., Holt, R.M. & Lozovyi, S. (2020) Stress paths and predicted time-shifts around a depleting reservoir [Expanded abstracts]. *90th SEG Annual Meeting*, Houston, TX, USA. SEG. pp. 2464–2468. <https://doi.org/10.1190/segam2020-3420041.1>

**How to cite this article:** Bakk, A., Duda, M., Xie, X., Stenebråten, J.F., Yan, H. & MacBeth, C. et al. (2024) Third-order elasticity of transversely isotropic field shales. *Geophysical Prospecting*, 1–25. <https://doi.org/10.1111/1365-2478.13446>

## APPENDIX A

### PATH STRAIN FOR A FIXED OFFSET

This appendix pertains to the axisymmetric model involving wave propagation along (assumed) straight ray paths in a vertical section  $[x_1, x_3]$  intersecting the reservoir's symmetry axis (Figure 6). When considering a fixed offset, where the horizontal distance between source and receiver remains the same in the baseline and monitor states, the seismic path length change between the source and the receiver is independent of the horizontal strain. Therefore, the  $e_1$  term is omitted from the path strain in Equation (40). In our scenario, the only nonzero shear strain ( $e_5$ ) results from the sum of two displacement gradients along  $x_1$  and  $x_3$ , respectively (Equation 2). Only the  $x_3$  component of the displacement gradient in  $e_5$  contributes to the path strain in a fixed offset scenario. Consequently, the longitudinal strain of the considered ray-path segment in Equation (40) transforms to

$$\bar{e}_{\text{RP,FO}} = e_3 \cos^2 \phi - \frac{1}{2} \frac{\partial u_3}{\partial x_1} \cos \phi \sin \phi. \quad (\text{A1})$$

By substituting  $\bar{e}_{\text{RP}}$  in Equations (42)–(44) with  $\bar{e}_{\text{RP,FO}}$  in Equation (A1), the two-way time shift, geometric contribution to the time-shift and time-strain are obtained for a fixed offset.